Spin Dynamics in the Time and Frequency Domain

Michael Farle, Tom Silva and Georg Woltersdorf

Abstract The current status of experimental approaches to analyze the spin wave dynamics in ferromagnetic nanoscale structures is reviewed. Recent developments in frequency- and field swept spectroscopy to determine the resonant response of nanoscale ferromagnets are described together with time-resolved measurements in the GHz frequency and pico second time domain, respectively. Examples for the analysis and manipulation of different mechanisms for the relaxation of the magnetization after microwave excitation into its ground state are presented.

1 Introduction

Dynamics (from Greek—dynamikos "powerful") in general refers to the time evolution of physical properties. In magnetism the term "spin dynamics" refers to the time evolution of the static macroscopic magnetization after thermal, electromagnetic (e.g. microwave) or matter wave/particle (e.g. neutron, electron or phonon) excitations. As the magnetization is the vector sum of all atomic magnetic moments—each containing an orbital and spin magnetic moment—(neglecting here the small nuclear magnetic moment which however is easily detected in magnetic resonance

M. Farle (✉)
Fakultät für Physik and Center for NanoIntegration Duisburg-Essen (CENIDE),
Universität Duisburg-Essen, Lotharstr. 1, 47057 Duisburg, Germany
e-mail: farle@uni-due.de

T. Silva
National Institute of Standards and Technology, Boulder, Colorado, USA
e-mail: silva@boulder.nist.gov

G. Woltersdorf
Department of Physics/ Magnetism Group, Universität Regensburg,
Universitätsstraße 31, 93040 Regensburg, Germany
e-mail: georg.woltersdorf@ur.de

H. Zabel and M. Farle (eds.), *Magnetic Nanostructures,*
Springer Tracts in Modern Physics 246, DOI: 10.1007/978-3-642-32042-2_2,

experiments, see for example [1]), one has to keep in mind that *orbital* dynamics which couples the spin moment to the crystal lattice is an important ingredient in spin dynamics. The orbital contribution is often hidden in a so-called effective spin model [2] or neglected due to its small contribution ($<10\,\%$) to the overall magnetization for example in 3d ferromagnets. In nanoscale structures, however, the contribution of orbital magnetism to spin dynamics may become important due to the increased percentage of magnetic moments which are located at surfaces and interfaces where they experience a low-symmetry electrostatic potential (crystal field) causing an enhanced orbital magnetic moment. Here, we will restrict our discussion to the model of effective spins or effective magnetization, respectively.

This chapter is organized as follows. We will begin with a short reminder on at first sight different manifestations of "spin dynamics" in ferromagnetic materials followed by a short overview of experimental techniques to record ferromagnetic resonance phenomena in materials with sub-micron dimensions. Magnetoresistive, microwave resonance, and optical detection schemes will be presented in a more detailed form in respective sections. This experimental part is preceded by a general discussion of the current understanding of how a magnetization relaxes to its ground state after resonant microwave or spin current excitation.

In spin dynamics—like in any other type of time evolution of a physical quantity—one has to consider the magnetic response in relation to the type (i.e. vector or scalar), amplitude and energy spectrum of the excitation as well as the relaxation rates and likely different dissipation channels allowing the stored energy to dissipate to the lattice. A wide energetic range of excitations produced by time varying magnetic fields has been investigated in the frequency and time domain of spin dynamics. Depending on the amplitude of the excitation linear- and non-linear magnetic responses which are described by the field- and frequency-dependent magnetic susceptibility tensor χ can be monitored. The phenomena can be subdivided into ultrafast magnetization processes (few tens to hundreds of femtoseconds) and processes evolving on the ps to ns timescale [3]. We will restrict our discussion to the later, that is resonant processes at $1 - 100\,\mathrm{GHz}$ frequencies.

The temperature dependence of the magnetization is governed by the thermally excited energy spectrum of elementary excitations of the magnetization called spin waves or magnons [4]—which are always present at finite temperatures (at 295 K there are app. $10^{21}-10^{22}$ cm^{-3} magnons). Spin waves follow dispersion relations [5] which depend on crystallographic orientation, size and shape of the ferromagnet [6, 7]. The dispersion relations for the spin wave vector ($\mathbf{q}$) covering momentum transfers over the full Brillouin zone and the energy range from μeV to several tens of meV (Stoner excitations), or that is in wavelength covering the range of tens of micrometers to nearest neighbor atomic distances, have been confirmed by experimental techniques like Brillouin Light Scattering (BLS) (see for example [8]), inelastic neutron scattering and energy loss spectrocopy (see for example [9]).

The term spin dynamics also covers the research areas of thermally induced "spin fluctuations" and "spin excitations" which for example become visible in the temperature dependence of the interlayer exchange coupling of two ferromagnetic layers coupled across a normal metal spacer layer like Cu [10], the temperature

dependence of the macroscopic magnetic anisotropy energy density (MAE) or at the para-ferromagnetic phase transition in form of the so-called critical broadening of the magnetic resonance linewidth at the Curie temperature (see for example [11]). A very straight forward way to see the effect of spin excitations is the temperature dependence of the magnetization at low temperatures ($T^{3/2}$ law). As evidenced in cubic nanoparticles the changes of the magnon excitation spectrum due to confinement are readily reflected in a modified temperature dependence of the macroscopic magnetization [12]. Also, it has been shown by scanning tunneling spectroscopy that the lifetime of a localized excited spin state of an Fe atom [13], which is a sensitive measure of magnetic dipole-dipole and exchange interactions with its local and distant environment, varies between 50 and 250 ns depending on its local coordination.

Available techniques cover the non-linear (large excitation amplitudes) and linear response regime. In the latter case the exciting microwave power is limited to a few tens of mW and the precession angle of the magnetization is only a few degrees. Ideally, only coherent precession of the magnetization is excited, that is to say we consider dispersion relations in the long spin wavelength (λ) limit that is $2\pi/\lambda = q \mapsto 0$. The discussion will be restricted to recent advances in modeling and experimental techniques, since the state of the art of measuring and modeling magnetization dynamics in confined magnetic structures has been described up to the year 2006 in three excellent books edited by B. Hillebrands and K. Ounadjela [14].

In recent years a number of time-resolved techniques have been developed with the aim to measure and image magnetization dynamics in magnetic micro and nanostructures. The magnetization state is probed using X-rays or light in the visible range. The contrast mechanism is X-ray magnetic circular dichroism or the magneto-optical Kerr effect respectively. While X-ray based techniques such a X-ray photoemission microscopy (XPEEM) or scanning transmission X-ray microscopy (STXM) [15] can have a spatial resolution as high as 20 nm, their time resolution is limited by the electron bunch length of the synchrotron to about 30 ps, i.e. a few GHz. Brillouin light scattering (BLS) (see for example [8, 16]) and time resolved Kerr microscopy (TRMOKE) [17] on the other hand can achieve only a moderate spatial resolution of 200–300 nm. The sub picosecond time resolution, however, allows to follow magnetization dynamics well into the THz regime [18]. Recent developments also include element-resolved spectroscopies in alloyed or composite ferromagnetic materials like X-ray Detected Magnetic Resonance (XDMR) [19] in which X-ray Magnetic Circular Dichroism (XMCD) [20, 21] can be used to probe the resonant precession of local magnetization components in a strong microwave pump field up to the THz regime and X-ray Resonant Magnetic Scattering (XRMS) which probes the motion of the magnetization stroboscopically as a function of time after magnetic field pulse excitation [22, 23].

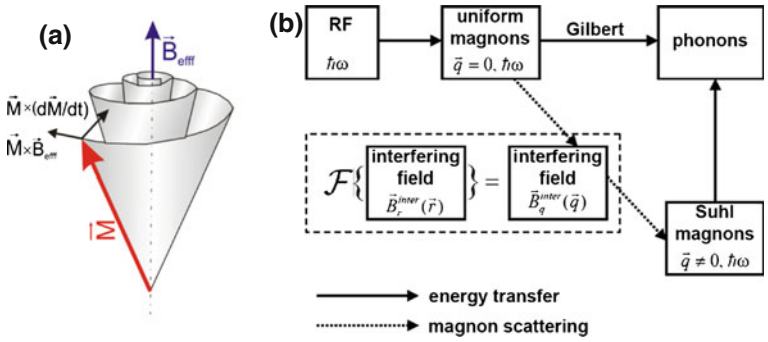

Fig. 1 **a** Simplified scheme showing the relaxation of the magnetization vector after microwave excitation. Restoring torques according to the Landau-Lifshitz-Gilbert equation are indicated. **b** Block diagram of the two most simple relaxation channels after microwave excitation. q is the wavevector of a magnon. Adapted from [24]

2 Energy Dissipation Channels for Reversal and Relaxation of the Magnetization

In general, one can say that the understanding of spin dynamics in nanomagnets requires a detailed knowledge of the precessional motion of the magnetization vector, involving the conditions for spin wave generation and dispersions and different relaxation channels after excitation. It involves various research areas in theory as well as in experiment (resonance, spin-torque, spin-injection, magnetic reversal, non-linear dynamics) to interpret the different modes of magnetic damping, relaxation and magnon scattering. Topics which will be touched upon involve linear versus non-linear processes, spin-spin versus spin-orbit driven mechanisms, frequency- versus time-domain measurements, ground state magnetism versus magnetism in an excited state. For all these mechanisms characteristic differences between metallic and insulating ferromagnets exist. Another interesting problem is the classification in dissipative and non-dissipative mechanisms in regard to the energy of the spin system.

We start very simply with the discussion of the relaxation of the magnetization by considering the phenomenological model of a precessing macroscopic magnetization of a ferromagnetic material Fig. 1a. In this model one considers a homogeneous magnetization which is the vectorial sum of initially collinear magnetic moments. The Larmor frequency of the precessional motion is well described by the Landau-Lifshitz equation from which the static magnetic properties appearing in the equation can be determined by angular- and frequency dependent FMR measurements. As discussed in [25] the resonance frequency ω is calculated by:

$$\left(\frac{\omega}{\mu_B g/\hbar}\right)^2 = \frac{1}{M^2 \sin^2(\theta)}\left[\frac{\partial^2 F}{\partial\theta^2}\frac{\partial^2 F}{\partial\phi^2} - \left(\frac{\partial^2 F}{\partial\theta\partial\phi}\right)^2\right] \tag{1}$$

where ω is the microwave frequency, g—the g-factor, ϕ and θ—azimuthal and polar equilibrium angles of the vector of magnetization M. Different forms of the free energy density functional F can be used. The following exemplary expression is valid for the geometry of an ultrathin film [25]:

$$F = -\mu_0 \mathbf{M} \cdot \mathbf{H}_{ext} - \mu_0 M\, H_\perp \cos^2\theta + K_2^{||} \sin^2\theta\ \sin^2\left(\phi - \phi_{K_2}\right) + K_4 \sin^2\theta - \frac{K_4}{8}\left(7 + \cos 4\phi\right)\sin^4\theta \tag{2}$$

that includes the Zeeman term, the perpendicular anisotropy field $H_\perp$, the in-plane uniaxial anisotropy $K_2^{||}$ with its easy axis defined by the in-plane angle ϕ_{K_2} and the cubic magneto-crystalline anisotropy K_4. The anisotropy fields K_i/M can be obtained with an accuracy of $<1\,\%$. The error of the anisotropy constants is dominated by the uncertainty of the saturation magnetization of $\leq 10\,\%$, evaluated from magnetometry measurements.

This analysis determines only the eigenfrequency of the uniform precession of the macroscopic magnetization, that is only the magnons with $\mathbf{q} = 0$. If one considers regionally non-collinear or in other words in time and space varying (out-of-phase) excited states, one can derive dispersion relations $\omega(q)$ for magnons which in the case of a thin film are for example given by [26] :

$$\omega = \gamma \left[\left(\mu_0 H + \mu_0 M_s \left(1 - \frac{1 - e^{-qd}}{qd}\right)\sin^2\phi_q + Dq^2 + H_{\mathrm{MAE1}}\right) \times \left(\mu_0(H + H_\perp) - \mu_0 M_s \left(1 - \frac{1 - e^{-qd}}{qd}\right) + Dq^2 + H_{\mathrm{MAE2}}\right)\right]^{1/2} \tag{3}$$

ω is a function not only of the wave vector q, but also of the external magnetic field H and sample parameters such as saturation magnetization M_s, effective perpendicular field $H_\perp$, spin wave stiffness D, film thickness d, the spectroscopic splitting factor $\gamma = \mu_B g/\hbar$, and parameters H_{MAE1} and H_{MAE2}, which are functions of very small anisotropy fields. Here, ϕ_q describes the angle between the magnetization and the spin wave vector. As explained in detail in Ref. [26] ϕ_q is very small, so that $\sin\phi_q \approx 0$.

The dynamic response of the magnetization is described by the equation of motion given by Landau and Lifshitz and the damping term suggested by Gilbert.

$$\frac{d\mathbf{M}}{dt} = -\gamma\left(\mathbf{M} \times \mu_0 \mathbf{H}_{\mathrm{eff}}\right) + \frac{\alpha}{M}\left(\mathbf{M} \times \frac{d\mathbf{M}}{dt}\right) \tag{4}$$

where $\mathbf{M}$ is the magnetization. The damping parameter α in SI units is related to the commonly used Gilbert damping factor G in CGS units by $\alpha = G4\pi/\mu_0 M\gamma$.

In a recent review by Fähnle et al. (see [3] and references therein) it was summarized that this phenomenological picture can be also understood in terms of electron-magnon scattering. It was calculated that the dominant contributions to the dissipative part of the dynamics in metallic ferromagnets arise from the creation of

electron-hole pairs and from their subsequent relaxation by spin-dependent scattering processes which transfer angular momentum to the lattice. Effective field theories (generalized breathing and bubbling Fermi-surface models) have been developed [3] which show that the Landau-Lifshitz-Gilbert equation of motion should be extended for the description of ultrafast magnetization processes, but in general provides an quantitatively excellent approach for the description of spin dynamics. Recently, Barsukov et al. [28] established by detailed frequency dependent FMR measurements and *ab initio* electronic structure calculations using the fully relativistic Korringa-Kohn-Rostoker Green's function method within spin-density-functional theory that the damping factor α is isotropic and depends on the composition in $Fe_{1-x}Si_x$ thin films. These films show for all compositions $0 < x < 40$ a very small composition dependent anisotropy K_4 (Fig. 2a). This may explain the observed and calculated isotropic behavior of α which in general should reflect the anisotropy of the orbital magnetic moment μ_l. As already pointed out by Kambersky (see [29] and references therein), for magnetic metallic systems two processes Eq. (5) for the relaxation of the net magnetization dominate the Gilbert damping factor G. Both *ordinary* and *spin-flip scattering* processes depend on the density of states at the Fermi level $N(E_F)$ and on the electron scattering time τ. They are directly proportional to the square of the deviation of the g-factor from its free spin-value [29]:

$$Spin - flip - scattering : G = \left(\frac{\gamma\hbar}{2}\right)^2 N(E_F)(g-2)^2/\tau \tag{5}$$

$$Ordinary - scattering : G = \left(\frac{\gamma}{2}\right)^2 N(E_F)\lambda_{SO}^2(g-2)^2/\tau \tag{6}$$

Since the magnetic anisotropy energy density is related to the anisotropy of the orbital magnetic moment $\delta\mu_l$ and since the g-factor measured in FMR (see for example [30]) is a measure of the orbital-to-spin magnetic moment ratio, one could hope to identify *anisotropic* Gilbert-type (spin-orbit) damping only in materials with large magnetic (uniaxial) anisotropy [31]. It must be noted, however, that the identification of such a intrinsic *anisotropic* Gilbert damping may be impossible due to the presence of the so-called two-magnon scattering which can also cause an angular dependent relaxation rate.

In a very simple scheme the relaxation channels of the excited magnetization can be described by the cartoon in Fig. 1b which dates back to discussions by H. Suhl recently reviewed in [32, 33]. The scheme indicates that uniform magnons with $\mathbf{q} = 0$—that is the uniformly precessing magnetization in Fig. 1a—are excited by microwave (RF) excitation. The uniform magnons can relax either via spin-orbit coupling and phonon-magnon interaction directly to the lattice or by dissipationless magnon-magnon scattering into non-zero wave vector magnon states followed by relaxation to the lattice. The intrinsic Gilbert damping path leads to heating of the lattice which for example can be used to detect magnetic resonance in a nanomagnet [34]. The other route indicated by the dashed arrow represents an initially dissipation free channel. Uniform magnons scatter into magnons with $\mathbf{q} \neq 0$ but with the same

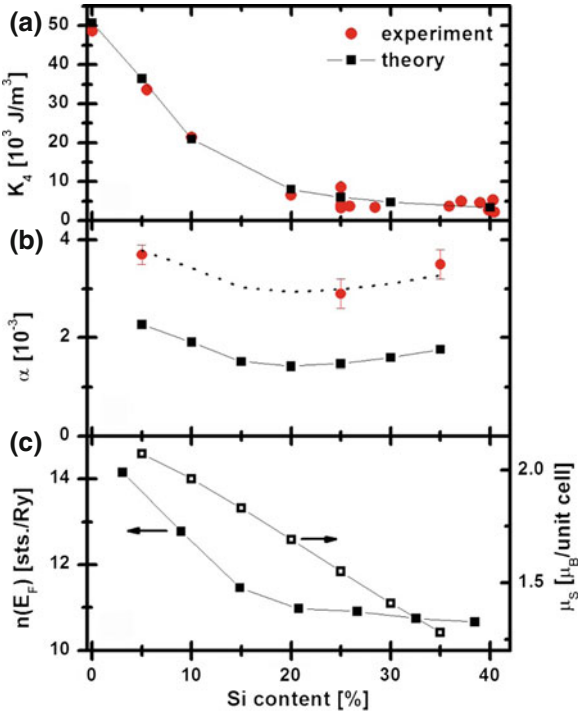

Fig. 2 Magnetic anisotropy energy and magnetic damping constant of Fe_{1-x} Si_x as a function of Si concentration. **a** Magneto-crystalline anisotropy constant K_4. Red dots show experimental data extracted from combined SQuID and FMR measurements on thin films grown on MgO(001). Error bars are 10 % due to the error in determining the magnetic volume. *Black dots* show the results of the DFT calculations for Fe-Si bulk-systems at 0 K. **b** Gilbert-damping parameter: *black squares* are results of the DFT calculation showing a minimum at $x \cong 20\,\%$. *Red dots* are experimental data obtained by frequency-dependent FMR measurements. *Dashed line* is a guide to the eye according to the theoretical data. **c** Average spin magnetic moment μ_s and electron density of states at the Fermi edge $n(E_F)$. The dependence on Si concentration correlates with the dependence of the Gilbert parameter. From [27]

energy $\hbar\omega$ as the $\mathbf{q} = 0$ state. Such a process is only feasible if the momentum transfer $\mathbf{q} = 0 \mapsto \mathbf{q} \neq 0$ is negligible and degenerate states in energy are available (compare Fig. 1b). The Suhl ($\mathbf{q} \neq 0$) magnons eventually lose their energy to the lattice. In the literature these two principally different relaxation channels are either referred to as intrinsic versus extrinsinc or Gilbert-type versus dissipation free channels. They are associated with different relaxation times T_1 and T_2 or in other words a longitudinal and transverse relaxation time as can be described by the Bloch-Bloembergen form of the Landau-Lifshitz equation:

$$\frac{dm_z}{dt} = -\gamma\,(\mathbf{m} \times \mu_0 \mathbf{H}_{\text{eff}})_z - \frac{m_z - M_S}{T_1} \tag{7}$$

$$\frac{dm_{x,y}}{dt} = -\gamma\,(\mathbf{m} \times \mu_0 \mathbf{H}_{\text{eff}})_{x,y} - \frac{m_{x,y} - M_S}{T_2} \tag{8}$$

In regard to the simple relaxation scheme of Fig. 1a one realizes that the dissipation free relaxation channel (dashed arrow) in the Scheme 1b results in a temporary decrease of the length of the magnetization vector associated with the transverse relaxation time T_2 or in other words a dephasing of the coherently precessing magnetic moments. A pure Gilbert type of relaxation would not lead to a change of the magnitude of the magnetization, and the tip of the vector would spiral along the surface of a sphere to its ground state. Finally, by annihilation of the Suhl magnons the system recovers its full magnetization given by the longitudinal relaxation time T_1.

The two-magnon scattering mechanism has been described theoretically by Arias and Mills [26, 35] based on the linear response theory and experimentally confirmed by several groups. In a two-magnon process a uniform magnon ($q_\parallel = 0$) initially created in a thin film with the magnetization lying in plane is scattered into a non-uniform state with the same energy and different wave vector $q_{\parallel S} \neq 0$, as shown in Fig. 3 (straight dotted line). Due to the local nature of this scattering process the momentum conservation can be violated [36]. In Fig. 3 the magnon dispersion for an ultrathin film magnetized in-plane including dipole-dipole interaction is shown. For the spin wave vector in-plane and parallel to the magnetization ($\phi = 0 < \phi_C$) the blue dispersion relation is obtained. Energetically degenerate states $q_{\parallel S}$ and $q_{\parallel 0}$ exist which can be coupled via the scattering potential F_{SCAT}. Usually, F_{SCAT} is given by randomly distributed defects in a thin film. If the angle ϕ between the in-plane direction of the magnetization and the wave vector increases beyond a critical angle ϕ_C, the degeneracy of the $q_{\parallel 0}$ and $q_{\parallel S}$ states is lifted, and the two-magnon scattering process becomes inoperative- allowing a straight forward identification in the experiment.

For applications that require certain relaxation times one wants to control the relaxation rate while maintaining the desired static magnetic properties of a material such as its magnetic anisotropy energy density, the saturation magnetization and interlayer exchange coupling. Some concepts for modifying the local damping in metallic ferromagnets, which unfortunately involve the risk of altering the static magnetic properties are:

- Doping with different elements [37–39]
- Ion mixing [40]
- Ion-induced segregation [41]
- Surface patterning of metallic layers by ion implantation [28]
- Formation of a regular defect pattern by oblique deposition in binary alloy films (e.g. Fe_3Si [42]).

An interesting possibility to minimize the unwanted changes of the static parameters of a ferromagnetic layer is the so-called spin-pumping effect [43]. By adding

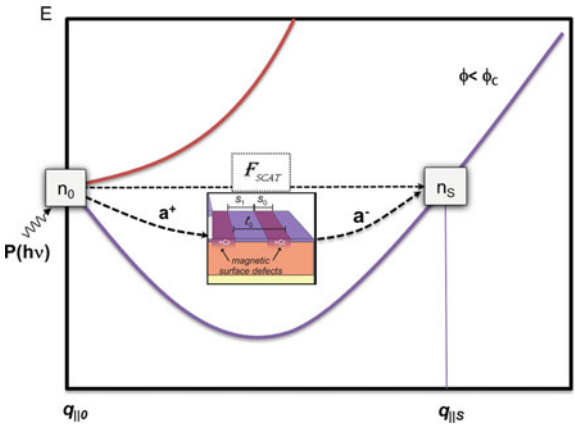

Fig. 3 Dispersion relation (including dipolar interaction) for magnons in a thin film. A number of uniform ($q_{||0}$) magnons are annihilated (a^-) and a number non-uniform magnons (n_S) with $q_{||S} \neq 0$ are created (a^+). This process is mediated by the scattering field F_{SCAT} which couples both magnon states. The number of uniform magnons (n_0) is increased by the microwave excitation and reduced by relaxation processes like the two-magnon scattering

a non-ferromagnetic metallic layer a spin-sink for a diffusive spin-current generated by the precessing magnetization after microwave excitation across the ferromagnetic/normal metal interface is created. Here, one has to be aware that this is a non-localized form of magnetic relaxation. The spin current carries away angular momentum from the ferromagnet into the normal metal where it is dissipated. Considerable effects have been seen in multilayered structures in which the relative orientation of two ferromagnetic layers separated by a normal metal layer determines the magnitude of the additional spin-pumping contribution to the intrinsic Gilbert damping [44]. The addition of the normal metal layer, however, may also modify the local crystalline structure by strain relief or creation [45] and thereby modify the static magnetic parameters like the magnetic anisotropy energy density.

Recently, a new approach for mesoscopically sized magnetic structures has been suggested based on the control of the two-magnon scattering mechanism. This approach realizes one possible route to extrinsically influence the longitudinal relaxation time—as indicated by the box of 'interfering fields" or scattering potentials for magnons in Fig. 1b. By artificially designing a periodic potential whose periodicity is adapted to the dominating magnon excitations the scattering rate can be enhanced and thereby the extrinsic or longitudinal relaxation time shortened. This is indicated in Fig. 3 by the scattering field F_{scat}.

The analysis of experimental FMR linewidths should at least include four different contributions ([46] and references therein):

$$\Delta B(\omega, \psi_B) = \Delta B^{\text{Gilbert}}(\omega, \psi_B) + \Delta B^{\text{mosaic}}(\omega, \psi_B) + \Delta B^{\text{2mag}}(\omega, \psi_B)\Delta B^{\text{inhom}} \tag{9}$$

Here ΔB denotes the peak-to-peak linewidth of the FMR signal. ψ_B denotes the two angles θ_B and ϕ_B, the first being the polar angle of the external field measured with respect to the film normal and the latter the azimuthal angle of **B** measured with respect to the in-plane [100]-direction.

The four different contributions to the FMR linewidth of Eq. (9) are:

(i) The Gilbert contribution $\Delta B^{\text{Gilbert}}$.
In various magnetic systems, the damping can be described by the phenomenological Gilbert damping parameter G. If the Gilbert damping represents the entire intrinsic damping, then it follows from the Landau-Lifshitz-Gilbert equation of motion that the FMR linewidth should depend linearly on the microwave frequency [31]. In order to determine G or α, frequency-dependent FMR measurements over a large range of microwave frequencies are needed. Note, that the linear frequency dependence of FMR linewidth is valid *only* when the magnetization and external magnetic field are parallel to each other. Otherwise the so-called field dragging contribution has to be included. If one wants to express relaxation rates in terms of linewidths, i.e. to convert from frequency-swept to the field-swept linewidth measured by FMR one can use the following conversion:

$$\Delta B(\omega, \psi_B) = \gamma \frac{dB_{\text{res}}(\omega, \psi_B)}{d\omega} \cdot \Delta\left(\frac{\omega}{\gamma}\right). \tag{10}$$

Here $\Delta(\frac{\omega}{\gamma})$ is the frequency-swept linewidth written in magnetic field units. The suffix 'res' indicates that $dB_{\text{res}}(\omega, \psi_B)/d\omega$ has to be calculated at the resonance condition. In Eq. (10) ω is a function of B and $\psi_B(B)$, therefore Eq. (10) can be written as

$$\begin{aligned}\Delta B(\omega, \psi_B) = {} & \gamma \frac{\partial B_{\text{res}}(\omega, \psi_B \equiv \text{constant})}{\partial \omega} \cdot \Delta\left(\frac{\omega}{\gamma}\right) \\ & + \gamma \frac{\partial B_{\text{res}}(\omega \equiv \text{constant}, \psi_B)}{\partial \psi_B} \cdot \frac{d\psi_B}{d\omega} \cdot \Delta\left(\frac{\omega}{\gamma}\right).\end{aligned} \tag{11}$$

The second term in Eq. (11) is commonly called the field-dragging contribution, because the partial derivative gets large at angles for which the magnetization **M** is dragged behind $\mathbf{B} = \mu_0 \mathbf{H}$ due to magnetic anisotropy effects. Along the hard and easy axes of magnetization, for which **M** and $\boldsymbol{\mu}_0 H$ are parallel, this dragging contribution vanishes. The Gilbert damping contribution in Eq. (9) is therefore given by:

$$\Delta B^{\text{Gilbert}}(\omega, \psi_B \equiv \beta) \approx \frac{2}{\sqrt{3}} \frac{\alpha}{\gamma} \frac{\omega}{\cos\beta} \tag{12}$$

where β is the angle between the magnetization $\mathbf{M}$ and external field $\mu_0\mathbf{H}$. For the in-plane configuration $\beta = \phi_{eq} - \phi_H$ and for the out-of-plane configuration $\beta = \theta_{eq} - \theta_H$.

(ii) Line broadening due to mosaicity (ΔB^{mosaic}).
The second term in Eq. (9) is the so called mosaicity term. It is caused by a small spread of sample parameters on a very large scale. This variation can be found in the internal fields, thickness, or orientation of crystallites within the sample. The individual regions thus have slightly different resonance fields. The overall signal will be a superposition of these local FMR lines yielding a broader linewidth. We consider the fluctuations of the *directions* of the anisotropy fields by the mosaicity contribution given by:

$$\Delta B^{\text{mosaic}}(\omega, \psi_B) = \frac{\partial B_{\text{res}}(\omega, \psi_B)}{\partial \phi_B}\Delta\phi_B + \frac{\partial B_{\text{res}}(\omega, \psi_B)}{\partial \theta_B}\Delta\theta_B \qquad (13)$$

where $\Delta\phi_B$ and $\Delta\theta_B$ represent the average spread of the direction of the easy axes in the film plane and normal to the film, respectively. Note that for frequency dependent measurements along the easy and hard axes the partial derivatives are zero and thus the mosaicity contribution vanishes.

(iii) The two-magnon scattering contribution $\Delta B^{2\text{mag}}$.
The two-magnon scattering is a process, where the $q = 0$ magnon excited by FMR scatters into degenerate states of magnons having wave vectors $q \neq 0$. This process requires that the spin-wave dispersion allows for degenerate states, and that there are scattering centers in the sample. The geometrical separation of the scattering centers is connected to the extension of the final magnon states in real space. If long wavelength spin-waves are involved in the relaxation process, defects of the order of several 100 nm rather than atomic defects act as scattering centers. The existence of two-magnon scattering has been demonstrated in many systems of ferrites.

The linewidth $\Delta B^{2\text{mag}}$ caused by the two-magnon scattering mechanism is a measure of the scattering rate of the uniform ($q = 0$) magnons into other spin-wave modes ($q \neq 0$). For a homogenously magnetized thin film, $\Delta B^{2\text{mag}}$ can be expressed as [47]:

$$\Delta B^{2\text{mag}}(\omega, \psi_B) \propto \sum_{\langle x_i \rangle} \Gamma_{\langle x_i \rangle} f(\phi_B - \phi_{\langle x_i \rangle}) \times \arcsin\left(\sqrt{\frac{\sqrt{\omega^2 + (\omega_0/2)^2} - \omega_0/2}{\sqrt{\omega^2 + (\omega_0/2)^2} + \omega_0/2}}\right) U\left(\theta_{eq} - \theta_c\right) \qquad (14)$$

with $\omega_0 = \gamma\mu_0 M_{\text{eff}} = \gamma\,(\mu_0 M - 2K_{2\perp}/M)$ and $\mu_0 M_{\text{eff}}$ being the effective magnetization that consists of $\mu_0 M$ and the intrinsic out-of-plane anisotropy field $2K_{2\perp}/M$. $\mu_0 M_{\text{eff}}$ can be determined by analyzing the angle dependent FMR resonance field. The factor $\Gamma_{\langle x_i \rangle}$ denotes the strength of the two-magnon scattering along the

principal in-plane crystallographic direction $\langle x_i \rangle$. This parameter will be fitted to the experimental data. The $f(\phi_H - \phi_{\langle x_i \rangle})$-term allows for the two-magnon contribution to depend on the in-plane direction of $\mu_0 \mathbf{H}$ relative to the principal in-plane crystallographic directions $\langle x_i \rangle$ given by the angles $\phi_{\langle x_i \rangle}$. An angle dependent two-magnon scattering may occur when the scattering centers are not isotropic within the sample. In the case that the centers are given by lattice defects, the angular dependence should reflect this lattice symmetry. In the case that different contributions of two-magnon scattering along the principal crystallographic directions $\langle x_i \rangle$ occur, one has to sum up these contributions weighted by their angular dependence given by f. The step function $U\left(\theta_{\mathrm{eq}} - \theta_c\right)$ in Eq. (14) is equal to 1 for $\theta_{\mathrm{eq}} > \theta_c$ and zero for $\theta_{\mathrm{eq}} < \theta_c$. It is used to describe the 'switching off' of the two-magnon scattering at a critical out-of-plane angle of the magnetization. Theoretically, it is shown that in oblique configuration, when the magnetization is tipped out of the film plane, finite wave vector modes are degenerate with the FMR mode for $|\theta_{\mathrm{eq}}| > |\theta_c| = 45°$. Thus the two-magnon scattering should be operative in this regime of the tipping angle, but it should shut off for $|\theta_{\mathrm{eq}}| < |\theta_c| = 45°$. It has been shown that the angular dependence of the two-magnon scattering can be approximated by a step function.

3 Ferromagnetic Resonance Detection in the Frequency Domain

3.1 Cavity Ferromagnetic Resonance

For macroscopic bulk samples Ferromagnetic Resonance has been measured using standard microwave technology based on microwave cavities working at fixed frequencies in a narrow band of about 1, 2, 4, 9, 26.5, 35 and 75 GHz (so called L-,S-, C-, X-, K-, Q- and W-band). The magnetic field part of the microwave field is perpendicular with respect to the external magnetic field which can be swept from 0 to 2.3 Tesla using electromagnets. The appearance of the resonance is observed by monitoring the reflected rectified microwave power from the microwave cavity. Setups for measurements of the Ferromagnetic Resonance (FMR) (or Electron Spin Resonance (ESR) for paramagnetic molecules) in ultrahigh vacuum have been developed (see [25] and references therein). For example, the temperature dependence of the magnetic properties of ferromagnetic monolayers under ultrahigh vacuum conditions, surface states (dangling bonds) at silica surfaces, and sub-monolayer coverages of paramagnetic molecules/atoms at low temperatures has been successfully analyzed [1, 48]. Standard cavity based spectrometers offer a detection limit of 10^{10} to 10^{14} paramagnetic moments with spin $S = 1/2$ provided the resonance linewidth is narrower than 10 mT [49]. This corresponds to a coverage of paramagnetic atoms or molecules on a cm^2 surface of 10^{-4} to 1 monolayer. Recently, the "cavity" concept was successfully miniaturized to the micron scale [50]. Due to the increased filling factor different spin wave modes in a single permalloy micron-sized stripe could be detected and quantitatively compared to the results of micromagnetic simulations.

This new approach offers currently an ultimate sensitivity of 10^6 magnetic moments corresponding to a nanoparticle of less than 100 nm diameter.

In the FMR experiment the presence of different relaxation channels (Fig. 1b) as discussed in the previous section is identified by the frequency dependence of the linewidth (ΔB) of the resonant spin precession [45, 46, 51]: The Gilbert damping exhibits a linear frequency dependence, whereas the two-magnon scattering follows the curved $arcsin$-like Eq. (14) behavior [26]. Although non-monotonous linewidth behavior had been considered for disordered polycrystalline systems previously [36], only recently (see for example references in [35, 52, 53]) systematic investigations on how to unambiguously identify and eventually control the two magnon relaxation mechanism have been published. Here we will discuss two examples beginning with the effects of a network of defects created in Fe_3Si ultrathin films by oblique deposition of the constituents. In the following chapter the frequency-selective enhancement of the magnetic relaxation rate by designing the periodicity of the defect structure will be demonstrated.

In [42] oblique angle deposition of Si during the deposition of 40 nm thick Fe_3Si epitaxial thin films on MgO(001) was used to create a network of defects with a preferential orientation. It could be demonstrated that this procedure created an effective scattering field for two-magnon scattering with 2-fold symmetry, whose preferential direction can be chosen by the deposition angle during film growth and whose scattering rate $\Gamma = 0.2$ GHz is comparable with the Gilbert damping of Fe_3Si in X-band. In Fig. 4 the experimental data which were extensively discussed and compared to theory in [42] are reproduced. By the uniaxial symmetry of the oblique deposition process an additional twofold contribution to the two-magnon scattering process can be controlled in magnitude and orientation by creating chemical disorder with a symmetry axis along any given in-plane direction and thus independently of the fourfold contribution from the network of unavoidable defects reflecting the cubic symmetry of the crystal lattice. The Si is deposited under an oblique angle of approximately 15° with respect to the film normal and the projection of the incident Si stream on the film plane is referred to as axis β (Fig. 4a). Such growth conditions are known to provoke so-called shadow effects.

Figure 4b shows the in-plane angular dependence of the resonance field B_{res} of a 40 nm thick film measured at 9.3 GHz and 295 K (Sample #2). Using the saturation magnetization $M_S = 0.96(8)10^6$ A/m measured by SQuID magnetometry, the effective perpendicular anisotropy field is $B_\perp \approx 1$ T and the in-plane magnetocrystalline anisotropy constant $K_{\parallel 4} \approx (3.3 \leftrightarrow 4.3)10^3$ J/m^3 can be calculated from the fit (solid line) to the data (red circles). The in-plane uniaxial anisotropy constant is small and amounts to $K_{\parallel 2}(0.1 \leftrightarrow 0.5)10^3$ J/m^3. Except for this small uniaxial anisotropy, a comparison with anisotropy values of the samples grown by non-oblique deposition reveals that the modified growth conditions do not considerably change the static magnetic parameters. However, there is a correlation of the in-plane uniaxial anisotropy $K_{\parallel 2}$ and the sample preparation. The hard axis of $K_{\parallel 2}$ is aligned parallel to the in-plane projection β of the Si flow. Indeed, stripelike defects caused by the shadow effect are known to induce such magnetic anisotropy in thin films by means

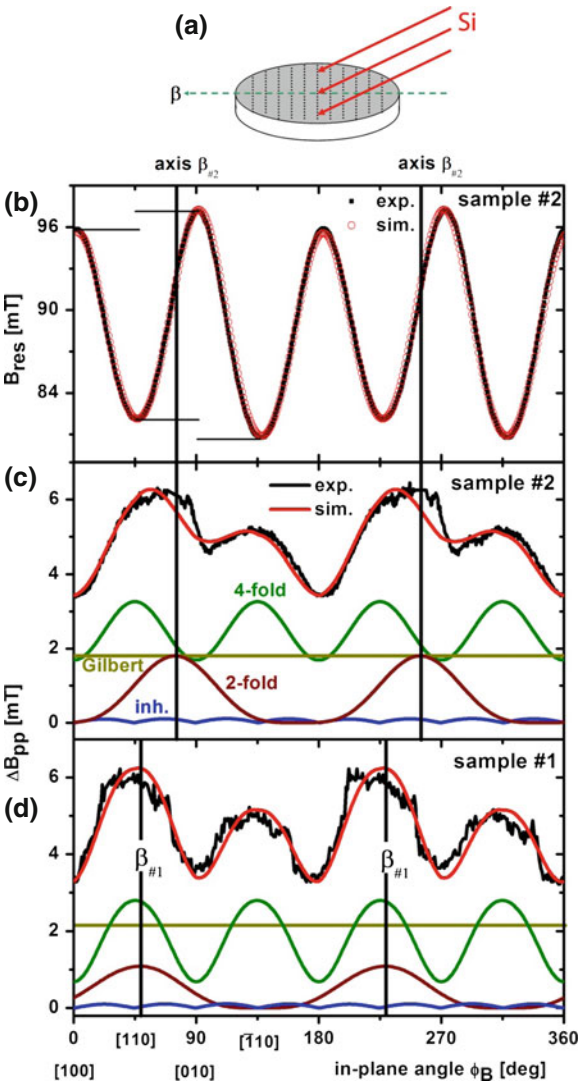

Fig. 4 **a** Sketch of the film deposition geometry. Oblique deposition of Si causes stripe-like defects with the symmetry axis perpendicular to the projection of the Si-flow β. **b–d**: 40 nm Fe_3Si/MgO(001) FMR data at 9.3 GHz. **b** In-plane angular dependence of FMR resonance fields, revealing the 4-fold crystalline anisotropy $K_{\parallel 4}$ and the small uniaxial anisotropy $K_{\parallel 2}$. FMR linewidth: **c** The native 4-fold contribution $\Gamma_{4\text{-}fold}$ caused by crystalline defects is superimposed by the 2-fold contribution $\Gamma_{2\text{-}fold}$. The maximum of the latter one is parallel to the hard axis of the uniaxial anisotropy and corresponds to the in-plane projection of the Si-flow: $\phi_{2\text{-}fold} = \phi_{uniax} = \beta$. **d** Linewidth of the sample #1, for which the axis β was set close to the [110] direction. From [42]

of the dipolar interactions among the defects. The low value of $K_{\parallel 2}$ suggests a low density of these defects.

The FMR linewidth ΔB_{pp} allows to identify the relaxation processes in the sample. In Fig. 4c the experimental linewidth (black line) is shown as a function of in-plane angle ϕ_B of the magnetic field. This in-plane angular dependence exhibits a behavior remarkably different from that of a regular film grown with a non-tilted Si evaporator [46]. While it has the typical fourfold symmetry of Fe_3Si/MgO(001) films, one also finds an additional *twofold* contribution superimposed. The latter

Table 1 Static and dynamic magnetic parameters (at X-band) of Fe_3Si/MgO(001) prepared under different growth conditions

Sample, Si deposition and film thickness	$K_4^{\|\|}$ (10^3 J/m^3)	$K_2^{\|\|}$ (10^3 J/m^3)	$\Gamma^{max}_{\langle 100\rangle}$ (10^7 Hz)	$\Gamma^{max}_{\langle 110\rangle}$ (10^7 Hz)	$\Gamma^{max}_{twofold}$ (10^7 Hz)	$\phi_{twofold}$ (deg)
#1 Oblique, 40 nm	4.0	0.2	51	13	20	49
#2 Oblique, 40 nm	3.8	0.5	58	30	33	74
#3 Oblique, 40 nm, not annealed	2.7	0.25	269	95	33	74
#5 normal, 40 nm (from Ref. [46])	3.3	–	53	26	–	–

Error bar of anisotropy constants: <10 %, of Γ^{max}_{ζ}: ~30 %, of $\Gamma^{max}_{twofold}$: <10 %, and of $\phi_{twofold}$: <5°

turns out to be of the same order of magnitude as the *fourfold* contribution and the Gilbert contribution. The simulation (red line) of the experimental ΔB_{pp} is the same as of the afore mentioned contributions to the FMR linewidth whose fitted angular dependences are shown by the green (*fourfold* two-magnon, extrinsic), brown (*twofold* extrinsic), blue (*inh* mosaicity, extrinsic) and yellowgreen (isotropic *Gilbert*, intrinsic) solid lines. The corresponding equations have been given in [42] and are not reproduced here. This angular dependence can be compared with the one of a nearly identical sample (#1) which was deposited with a change of the plane of incidence of the oblique Si stream. The angular dependence of ΔB_{pp} reveals the change of the plane of incidence from $\beta_{\#2}$ to $\beta_{\#1}$ (Fig. 4d). The calculated fit parameters for the magnetic anisotropy constants and two-fold and four-fold scattering rates are given in Table 1 in comparison to a non-annealed film and a film deposited with normal incidence of Si.

As shown in the Table 1, the modified growth conditions do also not affect the 4-fold two-magnon scattering process $\Gamma_{fourfold}$. Its intensity is comparable with results presented in [46]. The effective size of the rectangular, randomly located defects assumed for the fitting procedure lies in the range of few hundreds of nanometers—being plausible for the distance between crystalline defects in this system. Comparing the results of samples #1 and #3 reveals, that despite the modified growth the $\Gamma_{fourfold}$ intensity can be decreased by means of sample annealing.

3.2 Non-Cavity Approaches to FMR Detection

In this section we will briefly refer the reader to a selection of detection schemes of Ferromagnetic Resonance in the frequency domain which do not require the classical microwave cavity approach. The following list gives a few examples of such schemes.

- Ferromagnetic Resonance Force Microscopy [54]
- Photothermally Modulated Ferromagnetic Resonance (PM-FMR) for locally resolved and depth dependent measurements [55]

- Scanning Thermal Microscopy Ferromagnetic Resonance (SThM-FMR) [56], offering a lateral resolution of <100 nm and a sensitivity of 10^6 spins
- High-sensitivity broadband microwave spectroscopy with small non resonant coils [57]
- Broadband bolometric detection of resonant absorption in ferromagnetic nanoparticles [34]
- Broadband resonance detection of paramagnetic inclusions in weak links of Josephson junctions [58]
- Micro-resonators at fixed frequencies [50])
- Stripline and shorted wave guide based FMR techniques (see [51] and references therein).

Each of these schemes has certain advantages for specific materials and applications. Some of these techniques allow to sweep the frequency in a range of 1 to 10 GHz or even higher microwave frequencies, while in others the magnetic field is swept at constant microwave frequency. Also, one has to consider if one needs to characterize materials under ultrahigh vacuum (UHV) conditions, as a function of temperature, frequency and/or applied magnetic field strength/angle (see for example [25]). It is worthwhile to note that Kalarickal et al. [51] showed experimentally for three methods that frequency or field swept techniques yield the same FMR linewidth.

In the following we present a recent experimental result (Fig. 5) showing the possibility of manipulating the relaxation rate of permalloy films by introducing an artificial periodic scattering field F_{SCAT}. As described in detail in [28] a well-defined periodically modulated surface magnetization (scattering field F_{SCAT}, Fig. 3) of a permalloy film was prepared by low-dosage Cr implantation along stripes of width s_0 and separation s_1. In regard to the schematics in Fig. 3 one may expect to see characteristic changes in the relaxation rates due to extrinsic (*two magnon*) damping contributions. According to the theory developed by Landeros and Mills [59] increases of the FMR linewidth as a function of frequency are expected at characteristic spin wave vectors q_p reflecting the periodicity of the magnetization modulation. In Fig. 5 the first experimental observation [28] of this effect is shown. Using a newly developed shortened-coaxial-waveguide setup [60], which is UHV compatible, the FMR linewidth was determined in a quasi-continuous frequency range of 2 – 26 GHz. In Fig. 5a the experimental frequency dependence of the linewidth for the magnetic field applied parallel to the stripes with periodicity $l = s_1 + s_0 = 250$ nm is shown. The general behavior of the linewidth frequency dependence is not affected by the direction of the external magnetic field. The convex curvature is related to the high modulation field used to increase the signal-to-noise ratio. Additional measurements showed no isotropic two-magnon relaxation channel due to, e.g., grain-grain effects [61] in these polycrystalline samples. When the external magnetic field is applied perpendicular to the stripes, the behavior of the linewidth-frequency dependence becomes non-monotonous and is related to the two-magnon scattering process, which is known to be activated in such a configuration. One finds a large peak at 12.7 GHz and two smaller ones at 5.4 and 21.2 GHz. These appear only for the direction

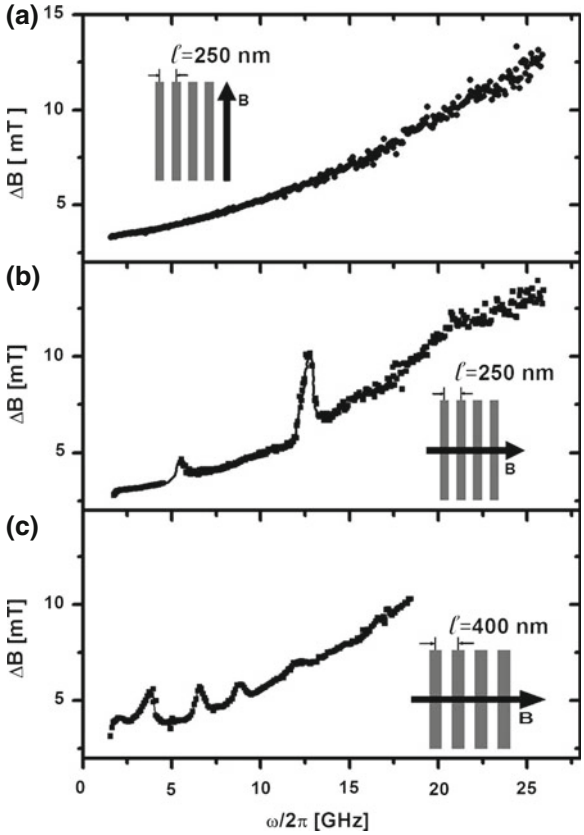

Fig. 5 Frequency dependence of the FMR linewidth of two samples structured with stripelike defects. While the general behavior is the same within one single sample for B parallel to the stripes (**a**) and B perpendicular to the stripes (**b**), for the latter configuration additional peaks due to the two-magnon scattering occur. Increasing the defects periodicity l from 250 to 400 nm in the second sample changes the position of the peaks and therefore the frequency dependence of the overall spin relaxation. In (**c**) the frequency range is limited due to technical reasons. *Solid lines* are guides for the eye

perpendicular to the stripes. Upon changing the periodicity to $l = 400\,\text{nm}$ the spacing of the relaxation rate (linewidth) peaks becomes smaller. This behavior is clearly distinct from the original monotonous arcsin-like Eq. (14) frequency dependence. In order to understand the appearance of these peaks one has to consider the dispersion relation of magnons parallel to the magnetization of a thin film Eq. (3). In a two-magnon process a uniform magnon with $q_{||_0}$ is scattered into a nonuniform state with the same energy and different wave vector $q_{||_S}$, as shown in Fig. 3. In order to find the wave vector of such a final-state magnon one needs to solve the equation $\omega(q_{||} = 0) = \omega(q_{||_S})$. The wave vector of the final-state magnons $q_S(\omega)$ can be calculated using the values of the effective perpendicular field, anisotropy fields, and

g factor. The scattering process itself is enabled by the scattering field, which couples the uniform with the final-state magnons. The coupling strength and consequently the FMR linewidth scale with the square of the Fourier transform of the scattering field for $q = q_S$. Using this model a very good qualitative agreement with the theory has been achieved [28].

3.3 Spin-Torque Ferromagnetic Resonance

Spin-torque ferromagnetic resonance (ST-FMR) is an alternative approach to measure spin dynamics in magnetic nanostructures [62–72]. The general approach is quite straightforward; an ac current is applied to a magnetic nanodevice that exhibits either giant magnetoresistance or tunneling magnetoresistance, and a dc voltage is generated that has a resonant structure when the ac frequency matches the resonance condition for FMR. The physical mechanism that gives rise to the dc voltage may be understood as follows. In a process commonly referred to as spin-momentum-transfer, or spin-torque, the non-equilibrium spin currents generated in such a device due to charge current flow between the different magnetic layers necessarily impart angular momentum to the magnetic layers in the device due to the sharp gradient in the spin current at the surface of a magnetic conductor.[1] The resultant ac torque at the surface of the magnetic layer gives rise to motion of the magnetization, thereby causing an ac variation in the device resistance. If the device resistance has a component that is in-phase with the ac current, rectification gives rise to a dc voltage. As will be shown below, the rectification is maximized when the excitation frequency approaches the FMR frequency, though the details of the voltage signal near resonance are strongly dependent on the symmetry of the spin torque in the structure.

Let U be the magnetic free energy for a rigid magnetic body. The equation of motion for magnetization $\mathbf{M}$ in a field $\mathbf{H} = -|\gamma|\left[\left(dU/dm_x\right)\hat{x} + \left(dU/dm_y\right)\hat{y}\right]$ is given by

$$\frac{d\mathbf{M}}{dt} = -|\gamma|\left[\mu_0\left(1+\alpha\hat{m}\times\right)\mathbf{M}\times\mathbf{H} - \frac{J_s}{\delta}\left(\varepsilon_\perp + \varepsilon_{||}\hat{m}\times\right)\hat{m}\times\hat{s}\right] \qquad (15)$$

where γ is the gyromagnetic ratio, μ_0 is the permeability of free space, α is the Landau-Lifshitz damping parameter, J_s is the transverse spin-current-density incident upon the magnet, δ is the thickness of the magnetic layer, $\varepsilon_\perp$ is the efficiency of the perpendicular, or "field-like" spin-torque, $\varepsilon_{||}$ is the efficiency for the parallel, or "damping-like" spin-torque, and $\hat{s}$ is the polarization direction of the spin-current.[2] The spin-current density has units of energy density, $\mathrm{J/m^3}$. For all-metal systems, it

[1] For a more detailed description of spin torque, see Chap. 2 by J. Lindner et al. in this book.

[2] A similar equation is presented in Chap. 2 by J. Lindner et al, though in terms of the Landau-Lifshitz-Gilbert damping phenomenology rather than the Landau-Lifshitz formulation employed here. In the limit of small damping, both equations are equivalent.

is generally understood that $\varepsilon_{\perp} \ll \varepsilon_{||}$. However, both data and theory indicate that $\varepsilon_{\perp}$ and $\varepsilon_{||}$ are of comparable scale for magnetic tunnel junctions (MTJs), though they have very different dependencies on the bias voltage applied across the tunnel barrier [69].

For the case of field-driven FMR (FD-FMR) with $J_s = 0$, an ac field $\mathbf{h}_{ac} = h_0 e^{-i\omega t}\hat{y}$, and $\mathbf{M} \cong m_x\hat{x} + m_y\hat{y} + M_s\hat{z}$, where $m_x, m_y \ll M_s$, the excitation torque-density $\mathbf{N}_{FMR} = \mu_0\mathbf{M} \times \mathbf{h}_{ac}$ is

$$\mathbf{N}_{FMR} \cong -\mu_0 M_s h_0 e^{i\omega t}\hat{x} \tag{16}$$

Thus, the excitation torque is necessarily at right angles to the excitation field. To understand the relationship of the magnetization to the excitation torque, we need to consider the small-amplitude motion of the magnetization as a function of excitation frequency, which can be easily derived from the Polder susceptibility tensor for the Landau-Lifshitz equation of motion,

$$\begin{pmatrix} m_x \\ m_y \end{pmatrix} = \chi \begin{pmatrix} h_x \\ h_y \end{pmatrix} \tag{17}$$

where

$$\chi \cong \frac{f_M}{f_0^2 - f^2 - if\Delta f} \begin{pmatrix} f_y + i\alpha f & -if \\ if_x & f_x + i\alpha f \end{pmatrix} \tag{18}$$

with $f = \omega/2\pi$, $f_M = |\gamma|\,\mu_0 M_s/2\pi$, $f_0^2 = f_x f_y$, $\Delta f = \alpha\left(f_x + f_y\right)$,

$f_{x,y} = |\gamma|\,M_s\left(d^2U'/dm_{x,y}^2\right)$, and U' does not include the excitation field.[3] If we consider the simplest high symmetry case with $f_x = f_y = f_0$ and $\alpha \ll f_{x,y}/f$, the equation of motion for the component of magnetization parallel to the applied ac field becomes

$$m_y = \frac{f_0 f_M h_0}{f_0^2 - f^2 - i2\alpha f f_0} \tag{19}$$

In the limit of $f \ll f_0$, we have $m_y = \left(f_M/f_0\right)h_0$; m_y is 180° out-of-phase with the excitation torque $\mathbf{N}_{FMR}$ along the x-axis, as depicted in Fig. 6. At resonance with $f = f_0$, we have $m_y = \left(i/2\alpha\right)\left(f_M/f_0\right)h_0$; m_y is 90° advanced relative to $\mathbf{N}_{FMR}$ and 90° retarded relative to $\mathbf{h}_{ac}$, but m_x is now 180° out-of-phase with N_{FMR}. The resonance condition is shown schematically in Fig. 6. This is an important general result of ferromagnetic resonance that is independent of the excitation source: $\mathbf{m}\cdot\hat{x}$ and $\mathbf{N}_{FMR}\cdot\hat{x}$ are anti-phased on resonance such that the excitation torque acts purely to counteract the damping torque, thereby maintaining a steady-state precessional

[3] This particular form of the susceptibility tensor presumes that $d^2U'/\left(dm_x dm_y\right) = 0$, i.e. the x and y coordinates have been chosen to lie along principal axes of the anisotropy, and the applied field is perpendicular to the $x - y$ plane.

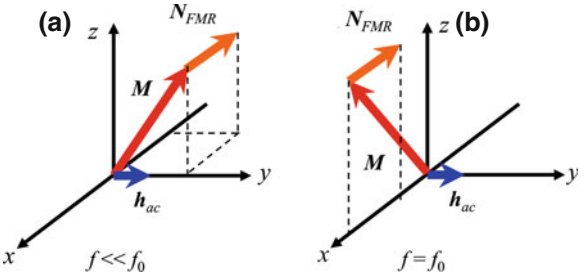

Fig. 6 Sketch of excitation torque acting on magnetization in field-driven FMR

orbit of maximum amplitude.[4] We will return to this point when we discuss the case of spin-torque FMR below.

The output signal for a field-driven FMR measurement depends on the type of detection method. If the detection is based upon an inductive measurement, then we have

$$V = i2\pi\mu_0 f A m_y \tag{20}$$

Now we will consider the case of spin-torque FMR (ST-FMR) with $\mathbf{h}_{ac} = 0$. The device structure now consists of two magnetic layers: A fixed reference layer that sets the direction of the spin current polarization, and an excited layer. Let us again assume small-amplitude magnetization motion of the excited layer about the saturation direction along $\hat{z}$. Let the polarization of the absorbed spin current $\hat{s}$ lie in the y-z plane, as depicted in Fig. 7. When the ac spin current is $J_{ac} = J_0 e^{-i\omega t}$, the excitation torque density $\mathbf{N}_{ST}$ is

$$\mathbf{N}_{ST} \cong \frac{J_0}{\delta}\left(\varepsilon_\perp \hat{x} + \varepsilon_{||}\hat{y}\right) e^{i\omega t} \tag{21}$$

This allows us to define an effective ac excitation field $\mathbf{h}_{ST}$ for the purposes of calculating the magnetization response, where

$$\mathbf{h}_{ST} = \frac{|\gamma| J_0 e^{i\omega t}}{2\pi f_M \delta}\left(\varepsilon_{||}\hat{x} - \varepsilon_\perp \hat{y}\right) \tag{22}$$

The relationship between the spin-current polarization vector $\hat{s}$ and the effective spin torque ac field $\mathbf{h}_{ST}$ is shown in Fig. 7. Let us now examine the signal produced by the spin-torque excitation. The output signal $V(t)$ due to giant magnetoresistance

[4] One must remember that the magnetization and angular momentum are antiparallel for electrons. Thus, a torque that is antiparallel to the magnetization will act to increase the magnetization along the torque.

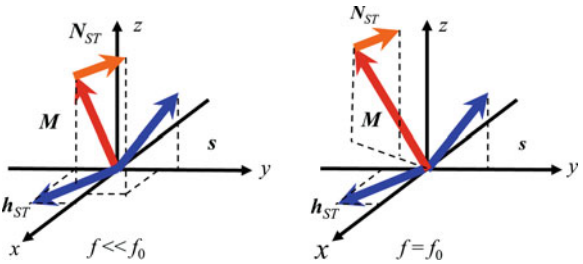

Fig. 7 Cartoon sketch of excitation torque acting on magnetization in spin-torque FMR

is given by

$$\begin{aligned} V(t) &= \left[\frac{Re\left[I(t)\right]\Delta R}{M_s}\right] Re\left[\mathbf{m}(t)\right]\cdot\hat{s} \\ &= \frac{1}{4}\frac{\Delta R}{M_s}\left[I(t)+I^*(t)\right]\left[m_y(t)+m_y^*(t)\right]\sin(\theta) \\ &= \frac{1}{2}\left(\frac{|\gamma|J_0 e^{i\omega t}}{2\pi f_M \delta}\cdot\frac{I_0\Delta R}{M_s}\right)\cos(\omega t)\left[\frac{f_M(if\varepsilon_{||}-f_x\varepsilon_\perp)}{f_0^2-f^2-if\Delta f}e^{i\omega t}+cc\right]\sin(\theta) \end{aligned} \tag{23}$$

where θ is the angle between the magnetizations of the reference layer (the presumptive source reservoir for the spin current) and the excited layer. The resultant voltage has a dc component V_{dc} given by

$$\begin{aligned} V_{dc} &= \frac{1}{2}\left(\frac{|\gamma|J_0}{2\pi F_M\delta}\cdot\frac{I_0\Delta R}{M_s}\right)\left[\frac{f_M(if\varepsilon_{||}-f_x\varepsilon_\perp)}{f_0^2-f^2-if\Delta f}+\frac{f_M(if\varepsilon_{||}-f_x\varepsilon_\perp)}{f_0^2-f^2+if\Delta f}\right]\sin(\theta) \\ &= \left(\frac{|\gamma|J_0}{2\pi\delta}\cdot\frac{I_0\Delta R}{M_s}\right)\left[\frac{\varepsilon_\perp f_x(f_0^2-f^2)+\varepsilon_{||}f_2\Delta f}{(f_0^2-f^2)+(f^2\Delta f)^2}\right]\sin(\theta) \end{aligned} \tag{24}$$

We immediately see that the parallel spin torque gives rise to an even-symmetry resonance response, whereas the perpendicular spin torque results in an odd-symmetry resonance spectrum. We can understand this quite easily since we know that the time-varying effective resistance is proportional to $\mathbf{m}\cdot\hat{y}$, and $\mathbf{N}_{ST}\cdot\hat{y}$ is 180° out-of-phase with m_y when on resonance. Thus, only the y-component of the spin torque contributes to the output signal when on resonance, resulting in a peak amplitude that is proportional to $\varepsilon_{||}$. Conversely, $\mathbf{N}_{ST}\cdot\hat{x}$ due to the perpendicular component of spin torque is 180° out-of-phase with m_x when on resonance, but any voltage signal due to $\mathbf{N}_{ST}\cdot\hat{x}$ is necessarily 90° out-of-phase with the excitation spin current, resulting in an odd-symmetry response curve.

An important prerequisite for the measurement of ST-FMR, as seen in the Eq. (24), is the mis-orientation of the active and reference layers. To accomplish this, various

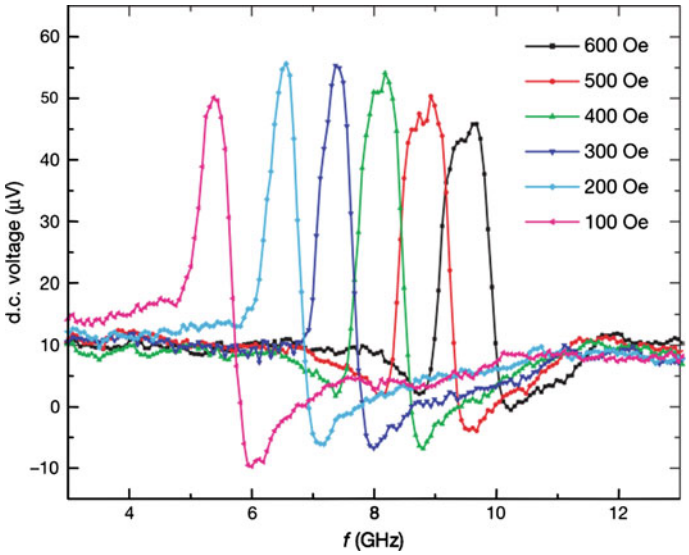

Fig. 8 Examples of the first ST-FMR spectra obtained with a magnetic tunnel junction device. The data show how the resonance frequency depends on an in-plane applied magnetic field, as expected for FMR. From Ref. [62]

approaches have been successfully used. For example, use of materials with greatly differing magnetic moment for the active and reference layers can result in strong misalignment of the magnetization orientation for the case of a perpendicular applied field.

While ST-FMR has yielded some of the first data for FMR in individual nanoscale magnetic structures, it suffers from inflexibility with regard to the thickness of the structure in question. This is immediately apparent in Eq. (24), where we see that the ST-FMR signal scales inversely with device thickness as a result of the interfacial nature of the spin-torque effect. Thus, only very thin devices are amenable to such measurements, leaving unanswered questions as to the role of phenomena such as spin-pumping in determining the overall damping in nanomagnets.

Spin-torque FMR was first demonstrated by Tulapurkar et al., by use of a 100×200 nm MgO-based magnetic tunnel junction (MTJ) device with a TMR ratio 100 % and a zero-bias, low-resistance of 150 ohms [62]. The applied magnetic field was in the film plane of the device. The device was excited at room temperature by ac currents ranging from 200 to 640 μA. The output dc voltage scaled quadratically with excitation current as expected for a rectification effect, and output signals as large as 35 μV were reported. Spectra were obtained by sweeping the excitation frequency, an example of which is shown in Fig. 8. The presented spectra exhibited a single peak at the resonance frequency with both even and odd symmetries, indicative of both the in-plane and perpendicular components of spin torque in the MTJ, as theoretically predicted for such devices [12]. The resonance frequency scaled with

applied dc magnetic field, and fitting of the data with the Kittel equation yielded an in-plane anisotropy of 176 Oe and an effective magnetization of 12.8 kOe. However, a dc bias voltage was not applied to the device, thus precluding any determination of the bias dependence for the different spin torque components in this particular device.

The first demonstration of ST-FMR in an all-metallic current-perpendicular-to-plane giant-magnetoresistive (CPP-GMR) device was reported by Sankey et al., for a 30×90 nm device with a 20 nm-thick Permalloy reference layer and a 5.5 nm-thick $Py_{65}Cu_{35}$ active layer [2]. The measurements were performed at cryogenic temperatures (<10 K), presumably to enhance the signal-to-noise ratio of the measurement. The applied magnetic field was out of the film plane and of sufficient strength to saturate the active layer magnetization out of the plane, while insufficient to do the same for the reference layer. The excitation currents ranged from 12 to 990 μA, and the maximum output signal was approximately 5 μV. Spectra were obtained by sweeping the excitation frequency, and multiple peaks were reported, indicative of multiple excitation modes in both the active and reference layers. In the absence of a dc bias current, the resultant spectra exhibited even symmetry about the resonance frequency at low ac currents. However, at high ac currents, the spectra acquired a distinct asymmetry that suggests nonlinear magnetization dynamics [9]. For these measurements, a dc current was also applied to modify the effective damping of the active layer, as shown in Fig. 9, which also includes an exemplary spectrum for zero dc current. Analysis of the data for linewidth vs. dc current yielded a zero-current damping of $\alpha = 0.04$ and a critical current ($\alpha = 0$) of $I_c = 0.4$ mA at an applied field of 0.535 T. Conventional room-temperature FMR measurements of unpatterned blanket films of the same composition as the active layer yielded a $= 0.021$. It was conjectured by the authors that the discrepancy in damping could be attributed to exchange coupling between the patterned active layer and an antiferromagnet oxide on the edges of the device that is below its blocking temperature for such cryogenic measurements. The absence of such extreme damping enhancement in subsequent room temperature measurements, as discussed below, corroborated this conjecture. However, an erroneous formulation for the dependence of the frequency-swept linewidth on damping was used for the data analysis. This was addressed in a subsequent publication from the same group, discussed below [66].

A theoretical treatment of ST-FMR in CPP-GMR devices was initially presented by Kupferschmidt et al. [64]. Their approach was to find a self-consistent solution of the charge- and spin-current propagation through a one-dimensional structure subject to appropriate boundary conditions. The methodology included an accounting for the reactive emission of spins from precessing ferromagnets into the nonmagnetic spacers, also known as spin pumping [43]. An important finding from the theoretical analysis was the contribution of the non-equilibrium spin accumulation in the nonmagnetic spacer layer to the dc voltage signal due to the generation of a nonzero dc chemical potential at the various ferromagnet/conductor interfaces within the device. It was determined that the contribution of the spin emission component to the net dc voltage signal was comparable to that due to simple rectification when the spin pumping component of the damping was of the same scale as the intrinsic damping.

To date, however, an experimental confirmation of this result remains lacking. A subsequent theoretical analysis by Kovalev et al., using similar methods, arrived at the same conclusion [65]. Another important result shared by both theories is the manifestation of an odd-symmetry component of the resonance even if $\varepsilon_{\perp} = 0$. The origin of the odd-symmetry is purely geometrical in origin, stemming from the possible misalignment of the effective spin-torque ac field $\mathbf{h}_{ST}$ with respect to the principle anisotropy axes of the device [64].

Fuchs, et al. first reported room temperature measurements for 50×10 nm all-metal CPP-GMR nanopillars [66]. An in-plane applied magnetic field was used. As was presented in the first work by the same group [63], the damping was inferred by measuring frequency-swept linewidth as a function of dc current, then using a linear fit to determine the zero-current linewidth. Since the dependence of frequency-swept linewidth on damping is proportional to the sum of the stiffness frequencies f_x and f_y, it is necessary to determine the effective anisotropy that establishes the FMR frequency. To see this, we consider the dependence of frequency-swept linewidth on damping,

$$\Delta f = \alpha(f_x + f_y) \tag{25}$$

where f_x and f_y are defined earlier in this chapter. Let us now consider the derivative of resonance frequency with respect to applied field,

$$\frac{df_0}{dH} = \frac{\gamma\mu_0}{4\pi f}(f_x + f_y) \tag{26}$$

Thus,

$$\alpha = \frac{\gamma\mu_0}{4\pi f_0}\frac{\Delta f}{\left(\frac{df_0}{dH}\right)} \tag{27}$$

We clearly see that determination of the damping from frequency-swept data is facilitated by a commensurate determination of the resonance frequency dependence on applied field. However, such data were not forthcoming in Ref. [66] which required an estimation of the stiffness frequencies by modeling the active elements as uniformly magnetized elliptical cylinders. The systematic errors associated with such an estimate were not determined. Nevertheless, the authors concluded that the extracted values for the zero-current damping were essentially identical (with 50 % error bars) to the measured values for unpatterned blanket films presented elsewhere in the literature.

A more accurate determination of damping in nanostructured CPP-GMR devices was presented by Chen et al. [67, 68]. This work used a Co/Ni multilayer active layer with perpendicular anisotropy, although the interfacial anisotropy was insufficient to overcome the intrinsic shape anisotropy for a thin film. The applied magnetic field was perpendicular to the film plane. The large difference in the net anisotropy

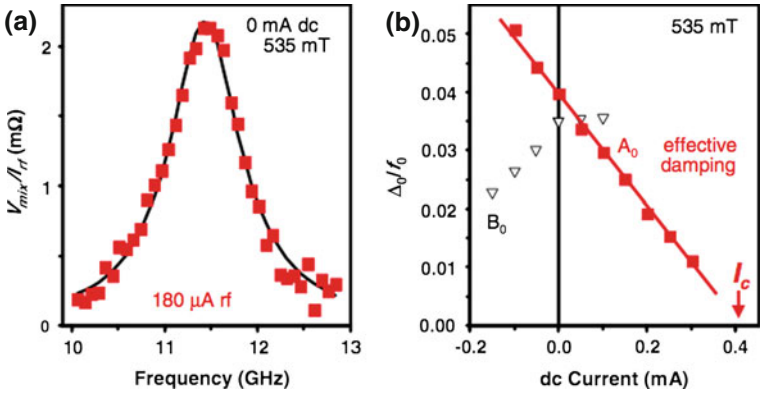

Fig. 9 Example of ST-FMR spectrum and dependence of spectral linewidth on dc current for metallic GMR device. **a** An example of a ST-FMR spectrum without any additional dc current. The applied field of slightly more than 0.5 T is oriented out of the film plane and is sufficient to saturate the excited layer out of the film plane. **b** The dependence of the ST-FMR linewidth on dc current. The observed linear dependence is in agreement with theoretical predictions (see Eq. 15). The critical current I_c for self-oscillations is extrapolated from a linear fit to the data. From Ref. [63]

of the active and reference layers allowed for the requisite misalignment of the magnetization angles over a wide range of applied magnetic field. Here, the field-swept linewidth was determined as a function of excitation frequency, permitting an unambiguous determination of the damping parameter as $\alpha = 0.033 \pm 0.003$, which was within error bars of a conventional FMR measurement for an unpatterned multilayer film with $\alpha = 0.036 \pm 0.002$. The linewidth vs. frequency data for both ST-FMR and FD-FMR are presented in Fig. 10. Similar to Fuchs et al., the authors concluded that patterning of the active layer nanomagnet did not cause a detectable change in the intrinsic damping. While micromagnetic simulations predict [73] and data have shown [74, 75] that multiple modes should be present in such finite-sized active layers, the experimental signal-to-noise was not sufficient to clearly determine the presence of such higher order modes. In addition, the shift of the device resonance frequency from that of the unpatterned film was approximately a factor of two less than what simulations predicted for the lowest order normal mode. The discrepancy between modeling and experiment was not explained, though it was conjectured that the actual device size may have been substantially different from the nominal dimensions of 50×150 nm.

The use of ST-FMR to study tunnel junction devices was revisited by Sankey et al. in an IBM/Cornell collaboration [69]. The devices under study (500×100 nm and 50×150 nm) utilized a CoFeB (3 nm)/MgO (1.25 nm)/CoFeB (2.5 nm) stack. In this case, the authors were less concerned with the damping of the active layer. Instead, the intention was to determine the dependence of the spin torque on bias voltage. It was observed that the ST-FMR lineshape exhibited both even and odd symmetry

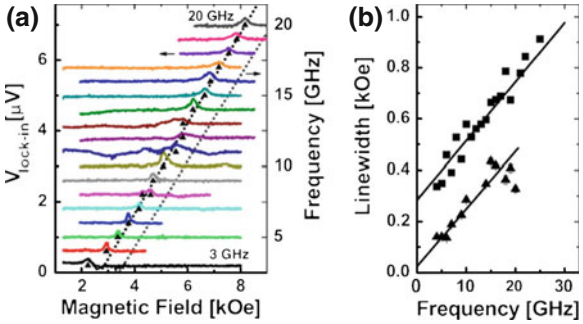

Fig. 10 Dependence of ST-FMR spectral peak position (**a**) and linewidth (**b**) on microwave frequency. The applied field is perpendicular to the plane of the device. The linewidth for FD-FMR is also shown in (**b**) with the filled square data points. The linewidth exhibits classic linear dependence on frequency, as expected for Landau-Lifshitz damping processes. From Ref. [67]

components Eq. (24) that had different dependencies on bias voltage. It was found that the parallel, or "damping-like", torque (referred to as the "in-plane" torque in Ref. [69]) only displayed a weak dependence on bias voltage for voltages as large as 0.4 V, even though the TMR ratio was reduced by a factor of two at such a bias voltage. In addition, the perpendicular, or "field-like", torque was comparable in magnitude to the parallel torque over the range of bias voltages, although its dependence on bias voltage appeared linear with a zero-intercept at zero bias.

Nonlinear resonance effects were indicated by Chen, et al. in another work from the NYU group that utilized CPP-GMR structures with Co/Ni active layers [70]. It was found that the field-swept resonance lineshape took on a distinctive "saw-tooth" shape with increasing microwave current excitation, as shown in Fig. 11. Such a lineshape results in a shift of the peak resonance frequency to lower applied magnetic fields with increasing microwave excitation. The saw-tooth shape is a tell-tale signature of nonlinear bistability in FMR measurements [76–78]. However, hysteresis of the lineshape, another essential feature of bistability, was very weak in comparison to macrospin simulation results. The authors speculate that thermally driven fluctuations might obscure the observation of such hysteretic effects.

ST-FMR has also been demonstrated with point-contact spin-torque devices, where the active layer is not lithographically patterned [71]. Instead, the current is injected into a blanket spin-valve stack using a lithographically defined point contact [79]. Again, the extracted value of damping was found to be in rough agreement with previously published results for the same material as the active layer, a Co/Ni multilayer with a net perpendicular anisotropy of only 64 mT. In addition, the determined ST-FMR resonance frequency dependence on applied field at zero bias current was found to coincide with the onset frequency of auto-oscillations at the critical current, demonstrating that the excitation generated by dc current in this particular device was of small amplitude at threshold.

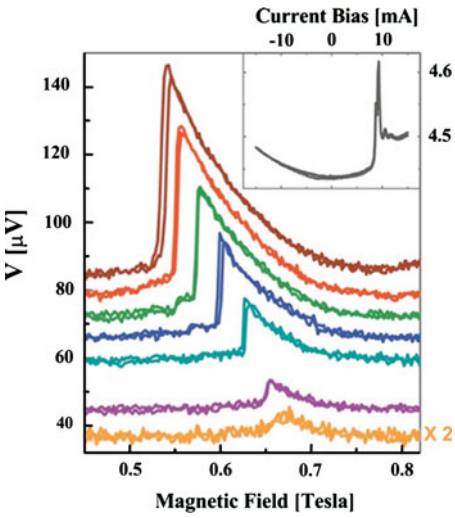

Fig. 11 ST-FMR spectra versus ac current amplitude for metallic GMR device. From *bottom* to *top*, the rf current amplitude was 1.4, 2.1, 3.3, 4.6, 6.2, 7.8, and 9.0 mA. The saw-tooth shape for large excitation amplitudes is evidence for large amplitude precession of the active layer magnetization. The shift in the peak resonance frequency from that for small excitation amplitude is linearly proportional to the decrease in the z-component of the magnetization at the maximum precession amplitude. From Ref. [70]

4 Ferromagnetic Resonance Detection in the Time Domain

4.1 Time Resolved Kerr Microscopy

Time resolved Kerr microscopy is a very convenient technique to study the magnetization dynamics in the time domain. In this method light from a pulsed laser is coupled into an optical microscope with polarization analysis. Due to the magneto-optic Kerr effect (MOKE) the polarization of light that is reflected from a magnetic sample is altered as a function of the orientation of the magnetization vector. Here this effect is used to study the dynamics of the magnetization vector in the sample. Time Resolved (TR)-MOKE is a pump-probe technique where the sample is periodically excited by an external stimulus (e.g. optical pulse or magnetic field pulse) which is synchronized to the laser pulses. The time resolution of such experiments is only limited by the duration of pump and probe events. For the experiments discussed in the following a Ti:sapphire laser is used to generate light pulses of 150 fs duration at a repetition rate of 80 MHz and at a central wavelength 800 nm. The laser light is split into two parts, which are referred to as pump and probe beams. The pump pulses are used to trigger magnetic field pulses which excite magnetization dynamics in the sample. The probe pulses sample the state of the system at a delay time Δt which is determined by the time delay between pump and probe pulse. In the present experimental setup the detection of the magneto optic Kerr effect is such that only the polar component of the magnetization vector contributes to the measured signal. However in principle it is possible to detect all components of magnetization vector in TR-MOKE experiments using a more sophisticated detection scheme [80]. In order to measure the time dependence of the magnetization an opto-mechanical

delay stage can be used to scan the optical path of the pump pulses with respect to probe events.

It is necessary to perform TR-MOKE measurements in a stroboscopic fashion since the signal of a single pump-probe event is too small to be detected. In order to obtain a sufficient signal to noise ratio the same experiment is typically repeated many million times at a fixed delay time while the pumping is modulated at a frequency of a few kHz. This modulation allows lock-in detection of the small dynamic Kerr signal. In addition, for experiments with pulsed excitation two conditions should be fulfilled. First, the relaxation of the system back into its ground state should be completed before the next pump pulse arrives. For the experiments discussed here the repetition rate of the laser is 80 MHz, i.e. this relaxation should take place within 12.5 ns. Second, the response of the system to the pump event has to be reproducible. All stochastic processes, such as variations of the response due to slightly different experimental conditions or thermal magnon excitation average out.

In the experimental setup the fundamental near infrared beam of the Ti:Sapphire laser ($\lambda \sim 800\,\text{nm}$) is focused into a lithium-borate (LBO) crystal, where the light is partly frequency doubled to $\lambda \sim 400\,\text{nm}$ by second harmonic generation. The spatial resolution $x_{\min}$ is obtained by scanning the sample laterally under the objective lens of a microscope using a piezo-mechanical stage. The resolution is diffraction-limited and determined by the numerical aperture of the objective lens and the wavelength of the light. The objective lens that is used has a numerical aperture of $\text{NA} = 0.90$. Therefore a spatial resolution of $x_{\min} = \frac{\lambda}{2\text{NA}} \approx 230\,\text{nm}$ can be achieved. The the polarization state of the reflected light is analyzed by means of a Wollaston polarizer and the difference signal is measured by two photo diodes. This difference signal is fed into a lock-in amplifier and sensitive to the time dependent magnetization state of the sample. In addition the intensity i.e. the sum signal of both photo diodes represents the reflectivity of the sample at the laser spot position. This signal allows to record the topography of the sample simultaneously with the magneto-optic response.

In the following sections experiments with pulsed and continuous wave (cw) excitation are discussed with the aim to illustrate the potential of the TR-MOKE technique.

4.2 Pulsed Experiments

In this section two experiments with pulsed excitation will be discussed. In the first experiment short current pulses are generated by optical pump pulses in a photoconductive switch. In a second experiment microwave bursts are generated by a signal generator. These rf-currents are coupled into a micro structured transmission line and the corresponding rf-magnetic field excites magnetization dynamics in the magnetic sample. The pump-probe experiments allow to record the ring down of the excitation by measuring the Kerr signal as a function of the delay time between pump and probe pulses. In the first experiment the interaction between a magnetic vortex

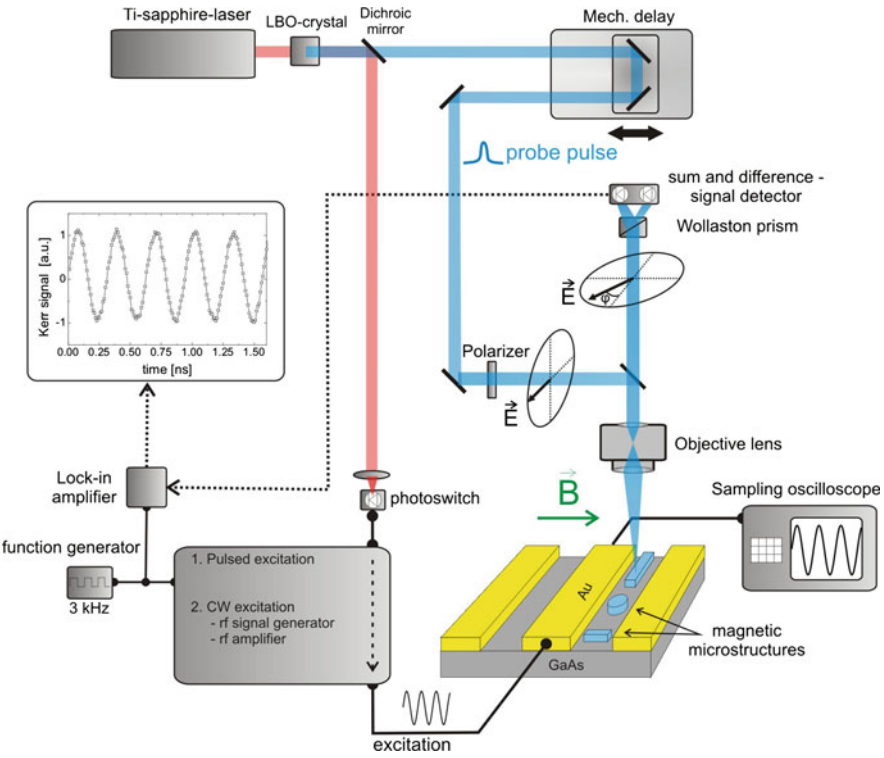

Fig. 12 Illustration of the time resolved Kerr microscopy setup. Part of the fundamental infrared beam of the Ti-Sapphire laser (∼800 nm) is frequency doubled using a LBO crystal. This frequency doubled blue beam (∼400 nm) probes the perpendicular magnetization component by means of the polar magneto-optic Kerr effect. The red laser pulses are delayed by means of a mechanical delay stage and focused onto a fast photo diode which triggers the generation of phase-synchronized microwaves. The microwave current passes through the coplanar waveguide structure of the sample, leading to an rf-magnetic field **h** which excites the precession of the magnetization. The sample is placed on a piezo scanning stage which is used to scan the sample laterally under the fixed laser focus. Static magnetic fields **H** can be applied in any direction in the sample plane by a rotatable electromagnet

core and spin wave eigenmodes in a magnetic disk will be examined. In the second experiment the propagation of spin-wave pulses which are excited by microwave bursts is studied.

4.2.1 Interaction Between Spin-Waves and a Vortex Core

In this experiment the magnetization in a disk of $Ni_{80}Fe_{20}$ with a diameter of 1.5 μm and a thickness of 15 nm is excited by in-plane magnetic field pulses. The current pulses which create an in-plane magnetic rf pumping field are generated by pulsed

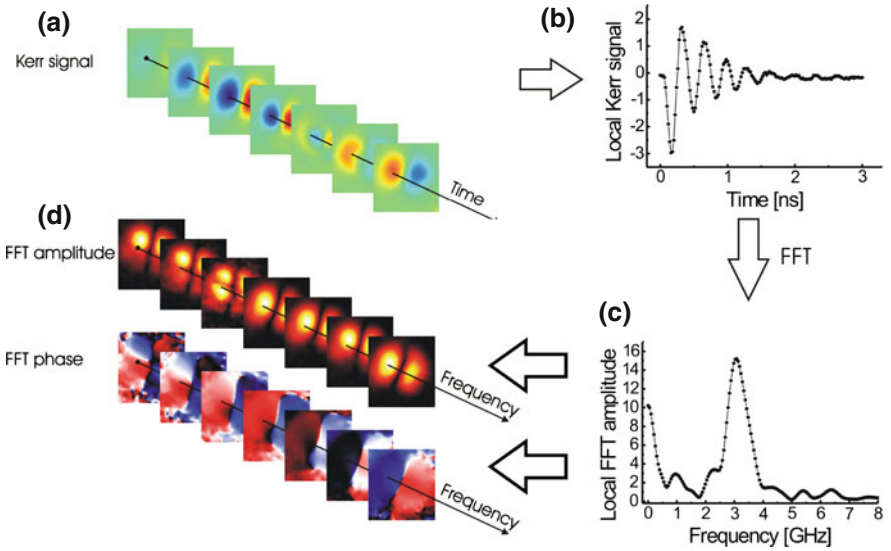

Fig. 13 Principle of imaging of eigenmodes by local Fourier transformations. **a** first a series of images of the Kerr contrast is recorded by TR-MOKE at various delay times after pulsed excitation of a $Ni_{80}Fe_{20}$ disk with a diameter of 1.5 μm and a thickness of 15 nm. Second the time dependence in each pixel of these images (shown in **b**) is Fourier transformed (**c**). **d** shows the amplitude and phase of the Fourier transformation (FFT) visualized as a function of frequency. Adapted from [82]

illumination of a photo-conductive switch as illustrated in Fig. 12 and the magnetic disk is placed on top of the signal line of a coplanar waveguide. The magnetization dynamics is recorded by TR-MOKE. For a given time delay between pump and probe pulses snapshots of the magnetic excitation as shown in Fig. 13a can be recorded. For each pixel of the snapshot the time evolution of the magnetic excitation can be plotted as can be seen in Fig. 13b. The application of a Fourier transformation to these time dependent data allows to identify the spin-wave eigenmodes [81]. In the frequency domain one can identify peaks corresponding to the excited eigenmodes (Fig. 13c). The amplitude and phase of the Fourier transformed spectra can be reassembled to form images as a function of frequency (see Fig. 13d). The eigenmodes are clearly visible. An in-plane field pulse applied to vortex state with its circulating magnetization mostly excites the first azimuthal mode $(1, \pm 1)$ as the $\mathbf{M} \times \mathbf{h}_{\mathrm{rf}}$ term has the opposite sign on both sides of the disk [82]. In addition also the magnetic vortex core is excited to gyrate around the center of the disk.

From the Fourier transformed data that were spatially averaged over one half of the disk as shown in Fig. 14a one can see that the intrinsic degeneracy of the clockwise and counter clockwise rotating first azimuthal modes $(1, +1)$ and $(1, -1)$ is lifted. In the amplitude and phase images at both peaks one can see that they correspond to the first azimuthal mode. However the phase of the lower peak rotates clockwise while the phase of the higher frequency peak rotates counterclockwise. This splitting is a

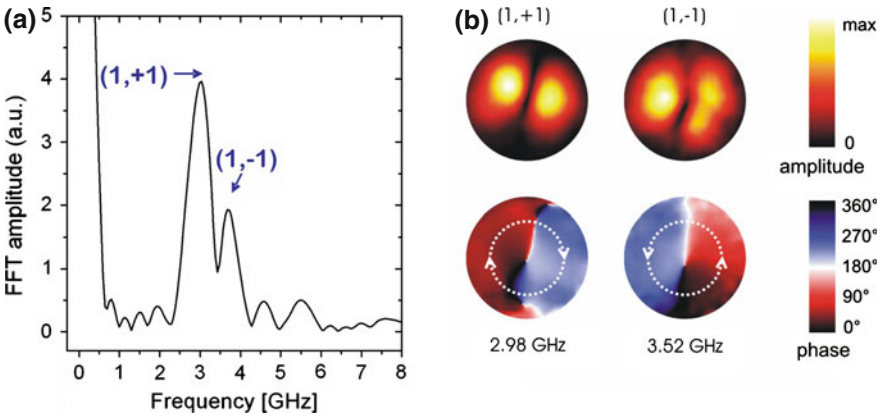

Fig. 14 **a** Fourier spectrum of measured dynamics averaged over one half of a $Ni_{80}Fe_{20}$ disk with a diameter of 1.5 μm and a thickness of 15 nm. **b** Spectral amplitude and phase images of the two azimuthal modes (1, +1) and (1, −1) measured by TR-MOKE. Adapted from [82]

consequence of the interaction of the spin-wave eigenmodes with the vortex core. We have demonstrated in [82] that the removal of the magnetic vortex core (by etching a hole in the center of the disk) results in a disappearance of the splitting. Guslienko et al. have shown theoretically that the dynamic interaction between the rotating spin-waves and the vortex core motion is responsible for the mode splitting [83].

4.2.2 Spin-wave Propagation

In order to study the propagation of spin-waves extended magnetic structures are needed. For this purpose this section discusses the propagation of spin-wave packets in large $Ni_{80}Fe_{20}$ film structures upon pulsed microwave excitation. Traditionally the spin-wave propagation and the propagation of non-linear spin-wave packets (bullets or spin-wave solitons) has been investigated mostly for the ferrimagnetic insulator Yttrium Iron Garnet due to its small intrinsic damping. In experiments employing inductive detection the propagation of spin-waves in ferromagnetic thin $Ni_{80}Fe_{20}$ films was observed over distances of up to 50 μm [84]. Here the direct TR-MOKE observation of the propagation of spin-waves in a 20 nm thick continuous $Ni_{80}Fe_{20}$ film is demonstrated.

The sample considered in the following consists of a 20 nm thick $Ni_{80}Fe_{20}$ film with lateral dimensions of 200 × 200 μm^2 patterned onto a GaAs substrate. Subsequently a coplanar stripline (CPS) is patterned over one edge of the $Ni_{80}Fe_{20}$ film using optical lithography (see Fig. 15a). A microwave generator is synchronized to the 80 MHz repetition rate of the Ti:Sapphire laser system in order to provide a phase-stable correlation between microwave excitation and the laser probe pulses. In addition a frequency mixer is added into the microwave circuit in order to generate

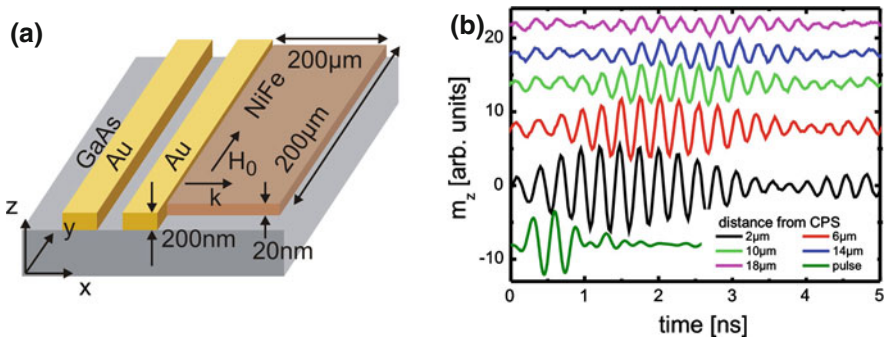

Fig. 15 **a** Sample layout. The 200 nm thick CPS fabricated from Au is placed over one edge of the $Ni_{80}Fe_{20}$ film. **b** Propagation of spin wave packets. Profile of the 4 GHz microwave pulse with a duration of 1 ns (*lowest line*) and scans in time of the spin wave packet at various distances from the CPS (the distance in microns is indicated above the individual lines). The curves have been offset for clarity. Adapted from [85]

microwave field pulses as short as 1 ns at a carrier frequency given by a multiple of the 80 MHz repetition rate of the laser. By measuring the Kerr signal as a function of delay time at various distances from the excitation source (waveguide) one can follow the propagation of a spin-wave packet directly. This allows one to observe the propagation of spin-wave packets in space and time as shown in Fig. 15b.

For a continously applied microwave excitation the response of the magnetization is given by the product of the q-dependent excitation and the q-dependent susceptibility. The q-vector where this product has a maximum is determined by the waveguide and the direction and magnitude of the applied magnetic field. This means that the magnetic film 'picks' the wave vector with the largest susceptibility from the Fourier spectrum of the CPS at a given driving frequency. By measuring line scans as a function of time the phase velocity v_{Ph} of the spin-waves can be directly determined from the slope $\triangle x/\triangle t$ of the oscillatory signal. The phase velocity can easily be converted into a q-vector: $q = \frac{2\pi f}{v_{Ph}}$. By performing such measurements as a function of frequency one can experimentally determine the dispersion relation for spin-waves [85].

When only short bursts of microwave excitation are applied to the sample one can study the propagation and dispersion of spin-wave pulses. Delay scans recorded at various distances from the CPS are shown in Fig. 15b. It can clearly be observed how the microwave burst triggers a spin-wave packet that propagates along the x-direction and broadens considerably as a function of time due to dispersion. In addition, the signal is damped according to the intrinsic damping parameter of the $Ni_{80}Fe_{20}$ film. Nevertheless, we are able to detect a response at distances up to 80 μm from the CPS. From these data of the pulsed excitation the group velocities of the spin-wave packets are readily determined. The measured group velocities $v_G = \frac{\partial \omega}{\partial q}$ are highest (up to 17 km/s) when the wave vector of the spin-wave and magnetic field are orthogonal (Damon Eshbach geometry), while they are smaller for intermediate field directions

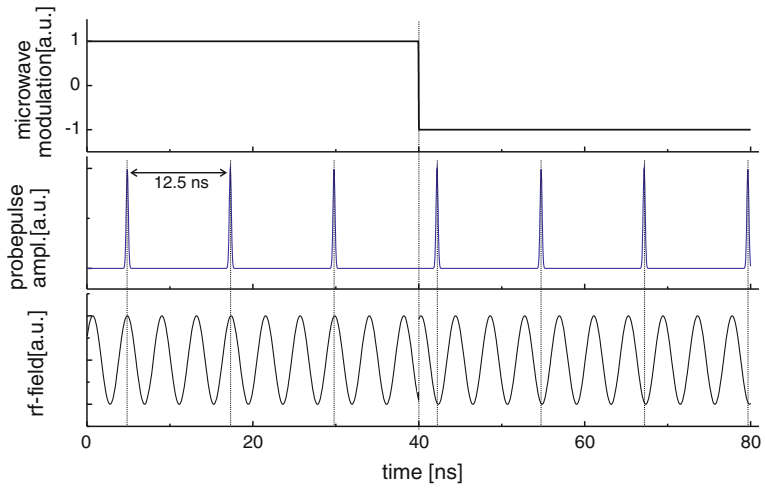

Fig. 16 Synchronization between continuous microwave excitation and laser probe pulses. Due to the repetition rate of the laser, the magnetization is probed every 12.5 ns. The microwave phase is the same for each probe event. 180° phase modulation of the microwaves is performed with a low frequency in the kHz-range. Note that at $t = 40$ ns, the phase of the excitation field is switched by 180°

and close to zero when q-vector and applied magnetic field are parallel (backward volume geometry).

4.3 CW Experiments: Ferromagnetic Resonance

Instead of applying a short magnetic field pulse or a microwave burst to the magnetic system the sample can be excited by means of a cw rf-field which is phase-locked to the laser pulses [86]. By measuring the TR-MOKE signal as a function of the time delay between microwave signal and optical probe one obtains the amplitude of the oscillating out-of-plane component of the precession. In addition, the phase of the response can be measured by comparing the phase of the Kerr signal to the phase of the microwave signal measured by a sampling oscilloscope.

For a fixed microwave frequency one can also measure ferromagnetic resonance (FMR) spectra by sweeping the external field. Depending on the relative phase between the probe pulses and microwave field, such FMR-TR-MOKE spectra are a combination or real and imaginary parts of the rf-susceptibility. The expected line shapes for real (in-phase) part χ' and imaginary (out-of-phase) part χ'' of the susceptibility are shown in Fig. 17. The static magnetization is assumed to point along the x-direction and the tip of the precessing magnetization is assumed to precess on a circular path in the y-z-plane due to the microwave excitation. The dots label the position of the tip of **M** at the point in time when the probe pulse samples the

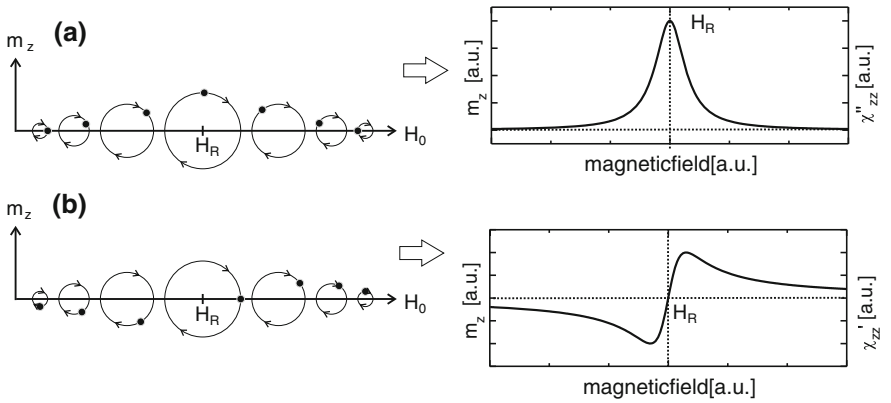

Fig. 17 Illustration of the different line shapes in Kerr-FMR measurements. (*Left side*) z-components of the magnetization m_z versus external magnetic field H for two different microwave phases. The static magnetization lies along the x-direction. The circles represent the precessing magnetization in the y-z-plane. The dots label the position of the tip of the magnetization vector for different field values at the moment when the probe pulses sample the polar component (m_z). (*Right side*) Depending on the phase correlation, the resulting spectra can have a symmetric (**a**) or an asymmetric line shape (**b**)

z-component of **M**. Far away from resonance ($H \ll H_R$ and $H \gg H_R$), the precession amplitudes are small, expressed by the smaller circles. At resonance ($H = H_R$), the precession amplitude is maximum. In addition, the phase between excitation field $\mathbf{h}_{\mathrm{rf}}$ and the precessing magnetization **M** has to be considered. For high magnetic fields, $\mathbf{h}_{\mathrm{rf}}$ and **M** move in phase ($\varphi = 0$), since the frequency of the microwave field excitation is much lower than the resonance frequency. The phase changes gradually from 0 to $\pi/2$ when the external field is decreased. At resonance, the phase lag of the precessing magnetization behind the excitation field is exactly $\pi/2$. In order to perform such measurements a microwave generator is synchronized with the laser pulses and an electronic line stretcher allows precise adjustment of the microwave phase. The rf-signal is delivered to the sample by a coplanar waveguide. In order to ensure both the excitation of the sample and the phase synchronization of the microwave signal with the probe laser pulses the microwave signal is monitored using a sampling oscilloscope. The synchronization between excitation and probe pulses is shown schematically in Fig. 16. Since the microwave phase is modulated by 180° (cf. Fig. 16), the output signal from the lock-in amplifier represents the difference signal of magnetization vector from opposite sides of the precession cone (cf. Fig. 17). TR-MOKE with cw excitation allows to combine two experimental techniques: ferromagnetic resonance (FMR) and time-resolved scanning Kerr microscopy. FMR-TR-MOKE allows one to perform spatially resolved resonance measurements. Thus this technique can be used to image magnetic modes in confined magnetic structures or to visualize local variations of the internal fields [87].

In the following the capabilities of this technique will be demonstrated by two examples. First this technique is used to measure the dynamics due to pure spin currents in metallic multilayers. In the second example local magnetic resonance spectroscopy is used to obtain the magnetic anisotropies in stained nano-structures of a magnetic semiconductor.

4.3.1 Spin Pumping in Magnetic Bilayers

In this section the FMR-TR-MOKE technique is used to study the magnetization dynamics due to pure spin currents. Spin polarized currents offer the possibility to exert a large torque on nano-magnets [88, 89]. In recent years current induced magnetization dynamics was successfully demonstrated in magnetic nanostructures [79, 90, 91]. Such current induced dynamics is mostly studied in spin valve structures using columnar nano-magnets. In a nonlocal crossed wire geometry even the switching of a magnetic nano-particle by a spin current was demonstrated [92]. In all these experiments the spin polarized currents are driven by charge currents. The precession of the magnetization in a ferromagnet which is in contact with a normal metal layer leads to the emission of a pure spin current into the normal metal [93]. This effect is known as spin pumping and leads to an increased damping for the magnetization dynamics in the layer that emits the spin current [94, 95].

In the FMR-TR-MOKE experiment that is discussed in the following it is shown that rf-precession can be excited by the absorption of a pure spin current which is generated by spin pumping. For this an epitaxial stack of layers consisting of Fe and Au grown on GaAs(001) is investigated. It is known that the magnetic layers in Au/Fe/Au/Fe/GaAs structures are dynamically coupled via spin pump and spin sink effects [17, 95]. In such a magnetic bilayer the magnetization dynamics in the presence of spin pump and spin sink effects can be described by the following coupled set of modified Landau-Lifshitz-Gilbert equations [95]:

$$\frac{d\mathbf{m}_i}{dt} = -\gamma_{\mu_0}\left[\mathbf{m}_i \times \mathbf{H}_{\text{eff}}\right] + \alpha_i\left[\mathbf{m_i} \times \frac{d\mathbf{m}_i}{dt}\right] + \alpha_i{}^{\text{SP}}\left[\mathbf{m}_i \times \frac{d\mathbf{m}_i}{dt} - \mathbf{m}_j \times \frac{d\mathbf{m}_j}{dt}\right] \tag{28}$$

where $\mathbf{m}_{1,2}$ are unit vectors along the instantaneous magnetization directions of the two ferromagnetic layers F1 and F2. The strength of the spin pump and spin sink effects is given by the parameter $\alpha^{\text{SP}} = g\mu_B \frac{g^{\uparrow\downarrow}}{M_s}\frac{1}{t_1}$, where t_1 is the thickness of F1, $g^{\uparrow\downarrow}$ (in units of e^2/h) is the real part of the spin mixing conductance [95] and μ_B is the Bohr magneton. The exchange of spin currents is a symmetric concept and the equation of motion for layer F2 can be obtained by interchanging the indices $i \rightleftarrows j$ in Eq. (28). The net spin current generated by layer F1 propagates away from the F1/N interface [93] and is absorbed at the N/F2 interface if N is thinner or comparable to the spin diffusion length (spin-sink effect) [96]. Conservation of angular momentum requires that layer F1 looses spin momentum which leads to an increase of the Gilbert damping parameter of layer F1. Subsequently, the spin current absorbed at the N/F2

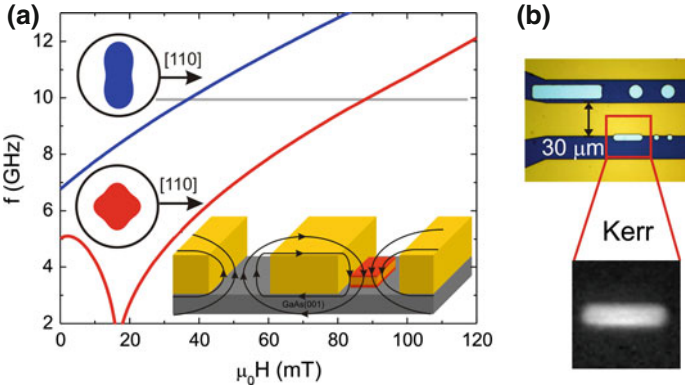

Fig. 18 **a** Calculated resonance frequency vs. applied field for 20Au/10Fe/250Au/16Fe/GaAs(001) (*numbers are in monolayers*) with the magnetic field applied along the [110] direction of Fe. The FMR frequencies for the 10Fe(F2) and 16Fe(F1) layers are shown in the *red* and *blue lines*, respectively. Note, that the *blue line* is shifted upwards compared to the *red line*. This shift is caused by the in-plane uniaxial interface anisotropy at the Fe/GaAs interface with the easy axis along the [110] direction. Layer F2 has a weak cubic anisotropy with easy ⟨100⟩ directions. Above 20 mT both layers are aligned parallel with their resonance frequencies separated by several GHz. The inset shows the experimental configuration. **b** Optical image of the actual sample. The signal line has a width of 30 μm. The magnification shows the Kerr signal of the 25 × 8 μm^2 rectangle in a bias field of 65 mT at a frequency of 8.08 GHz. From [17]

interface creates an rf-torque on the magnetic moment in F2. Since F2 is an ultrathin ferromagnet the interface torque results in a homogeneous precession of the layer F2 at the resonance frequency of F1. In an inductive FMR experiment this effect cannot be observed directly since the rf-response is dominated by the FMR signal from F1.

The single crystalline magnetic double layer structures that are used in the experiment are grown by molecular beam epitaxy in ultra high vacuum on GaAs(001) substrates, further details can be found in [94]. The different interface anisotropies of the two ferromagnetic layers can be used to split the resonance frequencies of F1 and F2 by several GHz. The expected resonance frequencies for F1 and F2 as a function of bias field applied along the [110] direction are shown in Fig. 18a. As shown in Fig. 18, for fields above 40 mT the magnetic moments of layers F1 and F2 and the dc field are collinear and parallel to the [110] direction of Fe.

A cw-signal of 10 GHz was applied to the micro structured coplanar transmission line (shown in Fig. 18b) and as expected from Fig. 18a the FMR-TR-MOKE signal for the layer F2 occurs at a field of 96 mT, as can be seen in Fig. 19a. At the resonance field of layer F1 a typical antisymmetric line (corresponding to the real part of the rf-susceptibility χ') and a symmetric line (corresponding to the imaginary part of the rf-susceptibility χ'') are found in the tails of the out-phase and in-phase rf-response, respectively. These signals at the F1 resonance field are in agreement with the spin pumping theory. F2 is driven by the spin current generated by F1, see Eq. (28), which is proportional to the time derivative of the rf-magnetization of layer F1.

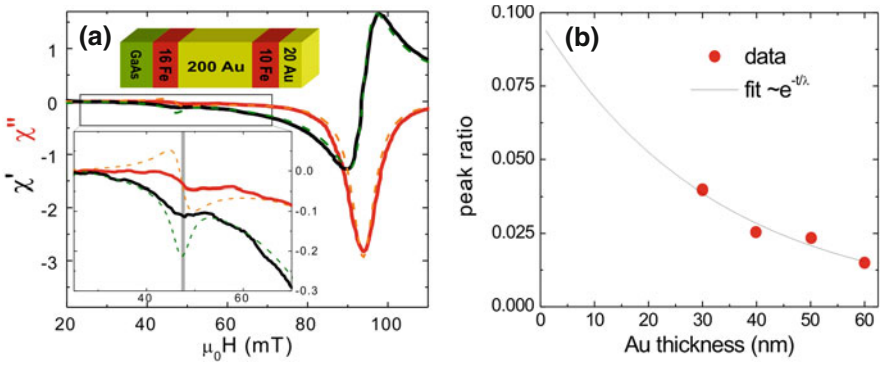

Fig. 19 **a** Measured real (*red line*) and imaginary (*black line*) parts of the perpendicular rf-susceptibility of layer F2. A frequency of 10 GHz was used and the magnetic dc-field was swept parallel to the [110] direction of Fe. The corresponding calculations using Eq. (28) are shown as *dotted lines*. The inset magnifies the region of interest. **b** The ratio of the signal amplitudes (FMR signal/ spin pumping signal) is plotted for a series of samples with Au spacer layer thicknesses between 30 and 60 nm. These data allow one to estimate of the spin diffusion length for Gold to be $\lambda_{sd} = 34$ nm. [97]

Therefore this driving is phase shifted by about $\pi/2$ with respect to the applied rf-field. Consequently, the additional driving due to spin pumping exchanges the resonance line shapes for the real and imaginary parts in the rf-susceptibility. I.e. in the imaginary (real) part of the F2 susceptibility has a contribution at the F1 resonance which has the line shape of the real (imaginary) part of the susceptibility of F1, see Fig. 19a. All these experimental features are well reproduced by the spin pumping theory using Eq. (28). The measured signal agrees with the calculations in its shape, however due to spin relaxation in the Gold spacer layer the amplitude is reduced by 70 % compared to ballistic spin transport, (c.f. dashed lines in Fig. 19a).

In the measurements the direct Kerr signal from the bottom layer is suppressed using an optical compensator [17]. In addition one should point out that dipolar coupling between the ferromagnetic layers e.g. caused by roughness would always lead to a symmetric line at the F1 resonance but cannot result in the observed antisymmetric line shape. Therefore one can firmly conclude that the signal measured at the F1 resonance in Fig. 19a is a sole consequence of the absorbed spin current in F2.

It is worthwhile to point out that the technique presented here can be used to estimate the spin diffusion length in the metallic spacer layer [17, 97]. For this the decay of the signal due to spin pumping is measured as a function of spacer thickness and compared to theory. This is shown in Fig. 19b. For the interpretation it is important to take spin diffusion effects into account [97]. The value one obtains for the spin diffusion length from these data at room temperature in Gold is $\lambda_{sd} = 34$ nm [97].

4.3.2 Local Magnetic Anisotropies

In this section it is shown that the FMR-TRMOKE technique can be used to determine the magnetic anisotropies with high spatial resolution. For this purpose measurements of the magnetic anisotropy of are performed in a spatially resolved manner on nanostructures of the magnetic semiconductor (Ga, Mn)As.

Due to the low Curie temperature of the diluted magnetic semiconductor, the experiments are carried out low temperature in a microscope cryostat. The magnetic properties of the diluted magnetic semiconductor (Ga, Mn)As have been studied previously using ferromagnetic resonance, SQUID, magnetotransport or Hall-effect measurements. In (Ga, Mn)As the magnetic anisotropies depend on temperature and hole concentration [98]. It was shown that the magnetic anisotropies can be manipulated by applying mechanical stress to the sample [99]. It has also been demonstrated that the easy axis of the magnetization can be rotated by varying the hole concentration using a strong electric field [100]. However, these techniques do not resolve magnetic anisotropies in (Ga, Mn)As micro-and nanostructures locally.

The experiments presented in the following show spatially resolved measurements of the magnetic anisotropy with a resolution of 500 nm. A (Ga, Mn)As film grown on GaAs(001) was investigated. Due to the lattice mismatch between (Ga, Mn)As and GaAs this sample is compressively strained. The strain gives rise to a strong perpendicular magnetic anisotropy with a hard axis along the film normal. By patterning a (Ga, Mn)As film into small structures this strain can be partially relieved, strongly affecting the magnetic anisotropies. The FMR-TR-MOKE approach combines the advantages of two experimental techniques: angle-dependent FMR provides direct access to the energy landscape and the magnetic anisotropies and TRMOKE microscopy allows spatially resolved measurements. Thus these experiments can serve to visualize local variations of the magnetic anisotropy.

In the following a 50 nm thick $Ga_{1-x}Mn_xAs$ film with a nominal Mn content $x = 0.06$ grown on a GaAs(001) substrate is studied. This sample has a Curie temperature of 170 K. Further details concerning the sample preparation can be found in [101]. The magnetic elements are defined by electron beam lithography and dry etching steps. The etch depth into the GaAs substrate is approximately 30 nm. Stripes having a width ranging from 200 nm up to 4 μm patterned along different crystallographic directions ([100], [110], [010]) and disks with different diameters were prepared. For the excitation of the magnetization with microwaves in the GHz-range a coplanar waveguide was defined in a subsequent lithography step. The magnetic elements are placed in the gap between the 30 μm wide signal line and the ground plane resulting in a out-of-plane rf-excitation, cf. Fig. 20a.

In order to determine the magnetic anisotropies FMR spectra are recorded for a series of applied field angles. Fig. 20b shows angle dependent FMR spectra for a large 60×60 μm^2 (Ga, Mn)As reference sample which represents the response of on an isotropically strained 'unpatterned' film. The individual TR-MOKE spectra are fitted to Lorentzian line shapes in order to determine the resonance fields. The resulting angular dependence of the resonance fields is shown in Fig. 20. By fitting this angular dependence the magnetic anisotropy constants in the free energy density can

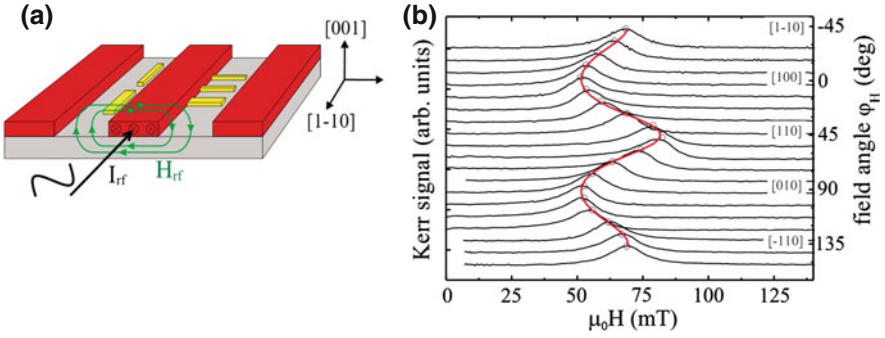

Fig. 20 **a** Sketch illustrating the waveguide and the rf excitation of the magnetic elements. **b** FMR spectra for various angles φ_H of the magnetic field in the film plane (001) for $f = 3.84\,\text{GHz}$ and $T = 7\,\text{K}$ for the reference structure. The resonance fields are obtained by fitting the experimental data to an asymmetric Lorentz function and are indicated by *open dots*. The *red solid line* represents the fit which is used to extract the anisotropy constants. From [101]

be determined [25, 101] : $F = -\mu_0 MH\,(\cos(\varphi_\text{M} - \varphi_H)) - \frac{1}{8}K_{4\parallel}(3 + \cos 4\varphi_\text{M}) - K_{2\parallel}\sin^2\left(\varphi_\text{M} - \frac{\pi}{4}\right)$, where M is the magnetization and φ_M and φ_H are the angles of the magnetization and the external magnetic field H with respect to the [100]-direction. $K_{2\parallel}$ and $K_{4\parallel}$ are the uniaxial and cubic in-plane anisotropy constants.

The angular dependence shown in Fig. 20b (isotopically strained film) is dominated by the intrinsic cubic anisotropy K_4. The difference in resonance field observed along the [110] and [1$\bar{1}$0]-directions is due to the in-plane uniaxial anisotropy $K_{2\parallel}$. The experimental data can be fitted well using the above energy density. The resulting anisotropy constants are $K_{4\parallel} = 2.2 \times 10^2 \frac{\text{J}}{\text{m}^3}$, $K_{2\parallel} = -1.1 \times 10^2 \frac{\text{J}}{\text{m}^3}$ and $K_{2\perp} = -3.0 \times 10^3 \frac{\text{J}}{\text{m}^3}$.

Next, the patterned (Ga, Mn)As structures are addressed. First we focus on narrow stripes. The four-fold symmetry of the reference sample shown in Fig. 20b changes into a pronounced two-fold symmetry when the (Ga, Mn)As film is patterned into a narrow stripe with a width of a few hundred nm (Fig. 21a). As the lattice can relax partially only along the side of the stripe for all three orientations of the stripes ([100], [010], [110]) the easy axis always coincides with the long axis of the stripe; in agreement with earlier studies using SQUID and magneto-transport measurements [102]. From these measurements we estimate the magnitude of the strain induced anisotropy $K_U = 1.8 \times 10^3 \frac{\text{J}}{\text{m}^3}$ for the 400 nm wide stripe. For narrow stripes (below a width of 500 nm) the induced anisotropy saturates since the strain can be fully relaxed across the stripe width. These results clearly demonstrate that the magnitude of the induced uniaxial anisotropy can be well adjusted by using stripe widths ranging between 500 nm and 1.5 μm.

In the following disk-shaped elements are addressed. The angular dependence of the resonance fields for a disk with a large diameter ($d = 10\,\mu$m, black symbols) and a small diameter ($d = 1.5\,\mu$m, red symbols) is shown in Fig. 22a. The experimental data for the 10 μm-diameter disk were obtained at the disk center where the strain

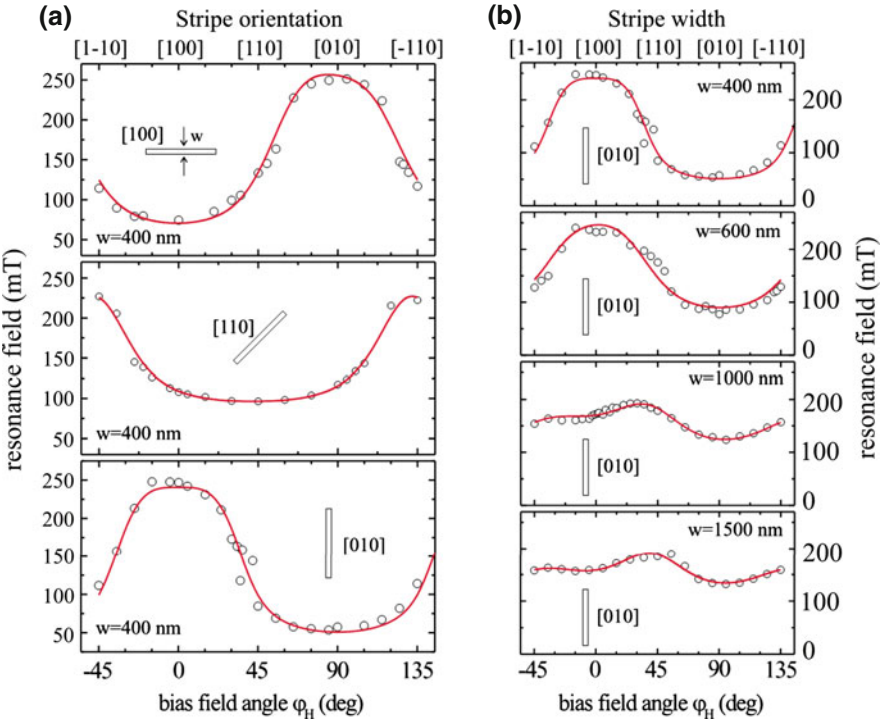

Fig. 21 Resonance field as a function of the external field angle φ_H for stripes patterned along different crystallographic axes (**a**) and different stripe width w (**b**). All data was obtained at $f = 7.2\,\text{GHz}$ and $T = 7\,\text{K}$. The solid lines are fits to the experimental data. From [101]

relaxation is almost zero. It should be emphasized that for a narrow rectangular structure the strain can only relax in one direction giving rise to a strong uniaxial anisotropy (Fig. 21a). For a disk-shaped element we expect isotropic strain relaxation. For this reason the in-plane anisotropies $K_{2\parallel}$ and $K_{4\parallel}$ should remain constant while the strain-induced perpendicular anisotropy $K_{2\perp}$ should be reduced. This reduction is indeed observed (Fig. 22a) as the resonance fields are only shifted to higher field values. The fits to the experimental data show that $K_{2\parallel}$ and $K_{4\parallel}$ remain almost constant while $K_{2\perp}$ is reduced by approximately 20 % for the disk with 1.5 μm diameter.

Finally we demonstrate the ability to visualize the local variations of the magnetic anisotropies for both the disk-shaped and the rectangular (Ga, Mn)As structures. Figure 22c–e show spatially resolved images of the Kerr signal obtained at a fixed excitation frequency f and applied field H. One finds laterally isotropic strain relaxation (indicated by the thick arrows in Fig. 22b). Furthermore one can distinguish two regions as illustrated in the figures: (i) the boundary of the structure where the strain relaxation takes place and a strong uniaxial strain induced magnetic anisotropy can be expected. And (ii) the central region of the structure where the (Ga, Mn)As

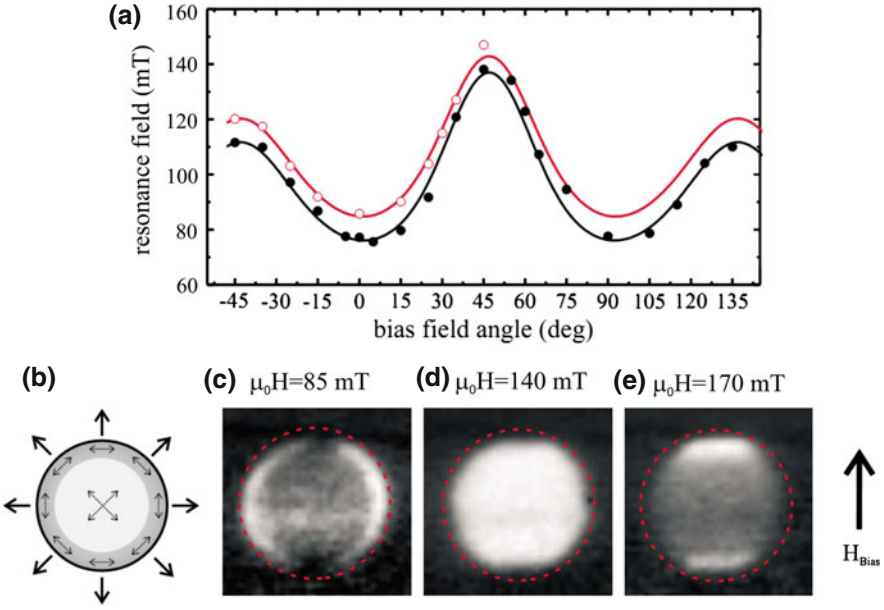

Fig. 22 **a** Angular dependence of the resonance field for disk-shaped (Ga, Mn)As elements for $f = 5.8\,\text{GHz}$ and $T = 7\,\text{K}$. The full *black* and the *open red dots* represent the experimental data for a disk with a diameter $d = 10\,\mu\text{m}$ and $d = 1.5\,\mu\text{m}$, respectively. The solid lines are obtained by fitting the experimental data. **c–e** Images of the polar Kerr signal for a disk-shaped element with a diameter of $10\,\mu\text{m}$ at a microwave frequency of $f = 5.8\,\text{GHz}$. From [101]

lattice remains fully strained and the magnetic anisotropy is unchanged compared to the extended (Ga, Mn)As film. As a consequence the magnetic anisotropies and the direction of the easy axes of the magnetization are varying locally. Based on previous results we expect the local easy axes (shown by the thin arrows) to be parallel to the boundary of the elements, whereas in the central region we expect the film-like behavior with easy axes along the ⟨100⟩-directions [101].

Spatially non-uniform magnetic anisotropies lead to a non-uniform magnetic response for uniform excitation. This behavior is clearly observed in Fig. 22c and e. The resonance field measured at the disk center (which for $\varphi_H = 45°$ is approximately $\mu_0 H_U = 140\,\text{mT}$, see Fig. 22a) leads to a uniform magnetic response (Fig. 22d). However for $H < H_U$ two ring shaped modes at the disk boundary (Fig. 22c) and for $H > H_U$ two modes localized at the edges are found (Fig. 22e). Note that while for $H < H_U$ these ring shaped modes are aligned along the field direction, for $H > H_U$ the modes are aligned perpendicular to H. The ring-shaped modes can be explained in the following way: Due to the lattice relaxation at the disk boundary the easy axis follows the circumference. Based on the results for narrow stripes where the easy axis of the magnetization prefers alignment along the long axis of the stripe we expect that the local easy axis is aligned tangentially to the boundary for curved elements like disks. For the ring shaped areas the external field

is aligned along the local easy axes which means that the resonance is observed at a lower bias field than the main resonance. In contrast for the areas located at the bottom and top of the image the bias field is aligned along a local hard axis, which results in a higher resonance field.

Acknowledgments This chapter is dedicated to the memory of Douglas L. Mills who lost his long battle with leukemia during the writing of this chapter. We thank all former and present co-workers—many of them appearing as co-authors of our publications—who have contributed to the results presented here. This work was supported by the DFG, Sfb 491. G.W. acknowledges financial support from the DFG through SFB 689 and project WO1422/2-1.

References

1. M. Zomack, K. Baberschke, Submonolayers of paramagnetic NO_2 adsorbed on Argon and Xenon films. Phys. Rev. B **36**, 5756 (1987)
2. A. Abragam, B. Bleaney, *Electron Paramagnetic Resonance of Transition Ions* (Oxford University Press, USA, 2012). ISBN 978-0-19-965152-8
3. M. Faehnle, C. Illg, Electron theory of fast and ultrafast dissipative magnetization dynamics. J. Phys. Condens. Matter **23**, 493201 (2011)
4. T.G. Phillips, H.M. Rosenberg, Spin waves in ferromagnets. Rep. Progr. Phys. **29**, 285 (1966)
5. A.I. Achiezer, V.G. Barjachtar, M.I. Kaganov, Spinwellen in ferromagnetika und antiferromagnetika. Fortschritte der Physik **10**, 471 (1962)
6. S.-K. Kim, Micromagnetic computer simulations of spin waves in nanometre-scale patterned magnetic elements. J. Phys. D Appl. Phys. **43**, 264004 (2010)
7. H. Puszkarski, Theory of surface states in spin wave resonance. Progr. Surf. Sci. **9**, 191–247 (1979)
8. B. Hillebrands, in *Brillouin Light Scattering from Layered Magnetic Structures*. vol. 75, ed. by M. Cardona, G. Gntherodt, Light Scattering in Solids VII, Topics in Applied Physics, (Springer, Berlin 2000), pp. 174–289. 10.1007/BFb0103386
9. Y. Zhang, P.A. Ignatiev, J. Prokop, I. Tudosa, T.R.F. Peixoto, W.X. Tang, Kh Zakeri, V.S. Stepanyuk, J. Kirschner, Elementary excitations at magnetic surfaces and their spin dependence. Phys. Rev. Lett. **106**, 127201 (2011)
10. S. Schwieger, J. Kienert, K. Lenz, J. Lindner, K. Baberschke, W. Nolting, Spin-wave excitations: The main source of the temperature dependence of interlayer exchange coupling in nanostructures. Phys. Rev. Lett. **98**, 057205 (2007)
11. Yi. Li, M. Farle, K. Baberschke, Critical spin fluctuations and Curie temperatures of ultrathin ni(111)/w(110): A magnetic-resonance study in ultrahigh vacuum. Phys. Rev. B **41**, 9596 (1990)
12. O. Margeat, M. Tran, M. Spasova, M. Farle, Magnetism and structure of chemically disordered $FePt_3$ nanocubes. Phys. Rev. B **75**, 134410 (2007)
13. S. Loth, M. Etzkorn, C.P. Lutz, D.M. Eigler, A.J. Heinrich, Measurement of fast electron spin relaxation times with atomic resolution. Science **329**, 1628 (2010)
14. K. Ounadjela, B. Hillebrands (ed.), in *Spin Dynamics in Confined Magnetic Structures I, II and III*. Topics in Applied Physics, (Springer, Berlin, 2002, 2004 and 2006)
15. A. Vansteenkiste, K.W. Chou, M. Weigand, M. Curcic, V. Sackmann, H. Stoll, T. Tyliszczak, G. Woltersdorf, C.H. Back, G. Schütz, B. van Waeyenberge, X-ray imaging of the dynamic magnetic vortex core deformation. Nat. Phys. **5**, 332 (2009)
16. V.E. Demidov, S. Urazhdin, S.O. Demokritov, Direct observation and mapping of spin waves emitted by spin-torque nano-oscillators. Nat. Mater. **9**, 984 (2010)

17. G. Woltersdorf, O. Mosendz, B. Heinrich, C.H. Back, Magnetization Dynamics due to Pure Spin Currents in Magnetic Double Layers. Phys. Rev. Lett. **99**, 246603 (2007)
18. A. Mekonnen, M. Cormier, A.V. Kimel, A. Kirilyuk, A. Hrabec, L. Ranno, T. Rasing, Femtosecond Laser Excitation of Spin Resonances in Amorphous Ferrimagnetic $Gd_{1-x}Co_x$ Alloys. Phys. Rev. Lett. **107**, 117202 (2011)
19. J. Goulon, A. Rogalev, G. Goujon, F. Wilhelm, J.B. Youssef, C. Gros, J.-M. Barbe, R. Guilard, X-ray detected magnetic resonance: a unique probe of the precession dynamics of orbital magnetization components. Int. J. Mol. Sci. **12**, 8797 (2011)
20. S. Pizzini, J. Vogel, M. Bonfim, A. Fontaine, in *Time-Resolved x-ray Magnetic Circular Dichroism : A Selective Probe of Magnetization Dynamics on Nanosecond Timescales*. vol. 87, ed. by B. Hillebrands, K. Ounadjela, Spin Dynamics in Confined Magnetic Structures II, Topics in Applied Physics, (Springer, Berlin 2003), pp. 157–187
21. H. Wende, Recent advances in x-ray absorption spectroscopy. Rep. Progr. Phys. **67**, 2105 (2004)
22. S. Buschhorn, F. Brüssing, R. Abrudan, H. Zabel, Precessional damping of fe magnetic moments in a feni film. J. Phys. D Appl. Phys. **44**, 165001 (2011)
23. R. Salikhov, R. Abrudan, F. Brüssing, St. Buschhorn, M. Ewerlin, F. Radu, I.A. Garifullin, H. Zabel, Precessional dynamics and damping in Co/Cu/Py spin valves. Appl. Phys. Lett. **99**, 092509 (2011)
24. I. Barsukov, R. Meckenstock, J. Lindner, M. Möller, C. Hassel, O. Posth, M. Farle, H. Wende, Tailoring spin relaxation in thin films by tuning extrinsic relaxation channels. IEEE Trans. Magn. **46**, 2252 (2010)
25. M. Farle, Ferromagnetic resonance of ultrathin metallic layers. Rep. Progr. Phys. **61**, 755 (1998)
26. R. Arias, D.L. Mills, Extrinsic contributions to the ferromagnetic resonance response of ultrathin films. Phys. Rev. B **60**, 7395 (1999)
27. I. Barsukov, S. Mankovsky, A. Rubacheva, R. Meckenstock, D. Spoddig, J. Lindner, N. Melnichak, B. Krumme, S.I. Makarov, H. Wende, H. Ebert, M. Farle, Magnetocrystalline anisotropy and gilbert damping in iron-rich $fe_{1-x}si_x$ thin films. Phys. Rev. B **84**, 180405 (2011)
28. I. Barsukov, F.M. Römer, R. Meckenstock, K. Lenz, J. Lindner, S. Hemken to Krax, A. Banholzer, M. Körner, J. Grebing, J. Fassbender, M. Farle, Frequency dependence of spin relaxation in periodic systems. Phys. Rev. B **84**, 140410 (2011)
29. V. Kamberský, Spin-orbital gilbert damping in common magnetic metals. Phys. Rev. B **76**, 134416 (2007)
30. A.N. Anisimov, M. Farle, P. Poulopoulos, W. Platow, K. Baberschke, P. Isberg, R. Wäppling, A.M.N. Niklasson, O. Eriksson, Orbital magnetism and magnetic anisotropy probed with ferromagnetic resonance. Phys. Rev. Lett. **82**, 2390 (1999)
31. W. Platow, A.N. Anisimov, G.L. Dunifer, M. Farle, K. Baberschke, Correlations between ferromagnetic-resonance linewidths and sample quality in the study of metallic ultrathin films. Phys. Rev. B **58**, 5611 (1998)
32. H. Suhl, Theory of the magnetic damping constant. IEEE Trans. Mag. **34**(4, Part 1), 1834–1838 (1998). 7th Joint MMM-Intermag Conference. (San Francisco, California, 1998), Jan. 06–09
33. K. Baberschke, in *Investigation of Ultrathin Ferromagnetic Films by Magnetic Resonance*. vol. 3, ed. by H. Kronmüller, S.S. Parkin, Handbook of Magnetism and Advanced Magnetic Materials, (Wiley, 2007), p. 1617. ISBN: 978-0-470-02217-7
34. I. Rod, O. Kazakova, D.C. Cox, M. Spasova, M. Farle, The route to single magnetic particle detection: a carbon nanotube decorated with a finite number of nanocubes. Nanotechnology, **20**, 19 (2009)
35. J. Lindner, I. Barsukov, C. Raeder, C. Hassel, O. Posth, R. Meckenstock, P. Landeros, D.L. Mills, Two-magnon damping in thin films in case of canted magnetization: theory versus experiment. Phys. Rev. B **80**, 224421 (2009)
36. C.W. Haas, H.B. Callen, *Magnetism*, vol. I (Academic Press, New York and London, 1963)
37. W. Bailey, P. Kabos, F. Mancoff, S. Russek. Control of magnetization dynamics in $Ni_{81}Fe_{19}$ thin films through the use of rare-earth dopants. IEEE Trans. Mag. **37**, 1749 (2001)

38. J.O. Rantschler, R.D. McMichael, A. Castillo, A.J. Shapiro Jr, W.F. Egelhoff, B.B. Maranville, D. Pulugurtha, A.P. Chen, L.M. Connors, Effect of 3d, 4d, and 5d transition metal doping on damping in permalloy thin films. J. Appl. Phys. **101**, 033911 (2007)
39. G. Woltersdorf, M. Kiessling, G. Meyer, J.-U. Thiele, C.H. Back, Damping by slow relaxing rare earth impurities in ni80fe20. Phys. Rev. Lett. **102**, 257602 (2009)
40. J.-M.L. Beaujour, A.D. Kent, D. Ravelosona, I. Tudosa, E.E. Fullerton, Ferromagnetic resonance study of Co/Pd/Co/Ni multilayers with perpendicular anisotropy irradiated with helium ions. J. Appl. Phys. **109** (2011)
41. C. Bilzer, T. Devolder, C. Chappert, O. Plantevin, A.K. Suszka, B.J. Hickey, A. Lamperti, B.K. Tanner, B. Mahrov, S.O. Demokritov, Ferromagnetic resonance linewidth reduction in feau multilayers using ion beams. J. Appl. Phys. **103**, 07B518 (2008)
42. I. Barsukov, P. Landeros, R. Meckenstock, J. Lindner, D. Spoddig, Z.-A. Li, B. Krumme, H. Wende, D. L. Mills, M. Farle, Tuning magnetic relaxation by oblique deposition. Phys. Rev. B **85**, 014420 (2012)
43. Y. Tserkovnyak, A. Brataas, G.E.W. Bauer, Spin pumping and magnetization dynamics in metallic multilayers. Phys. Rev. B **66**, 224403 (2002)
44. X. Joyeux, T. Devolder, J.-V. Kim, Y. Gomez De La Torre, S. Eimer, C. Chappert, Configuration and temperature dependence of magnetic damping in spin valves. J. Appl. Phys. **110** (2011)
45. J. Lindner, K. Baberschke, Ferromagnetic resonance in coupled ultrathin films. J. Phys. C **15**, S465 (2002)
46. Kh. Zakeri, J. Lindner, I. Barsukov, R. Meckenstock, M. Farle, U. von Hörsten, H. Wende, W. Keune, J. Rocker, S.S. Kalarickal, K. Lenz, W. Kuch, K. Baberschke, Z. Frait, Spin dynamics in ferromagnets: Gilbert damping and two-magnon scattering. Phys. Rev. B **76**, 104416 (2007)
47. Kh. Zakeri, J. Lindner, I. Barsukov, R. Meckenstock, M. Farle, U. von Hörsten, H. Wende, W. Keune, J. Rocker, S.S. Kalarickal, K. Lenz, W. Kuch, K. Baberschke, Z. Frait, Erratum: Spin dynamics in ferromagnets: Gilbert damping and two-magnon scattering [phys. rev. b 76, 104416 (2007)]. Phys. Rev. B **80**, 059901 (2009)
48. M. Yulikov, M. Sterrer, T. Risse, H.-J. Freund, Gold atoms and clusters on MgO(100) films; an epr and iras study. Surf. Sci. **603**(10–12), 1622–1628 (2009)
49. M. Farle, M. Zomack, K. Baberschke, ESR of adsorbates on single crystal metal surfaces under UHV conditions. Surf. Sci. **160**(1), 205–216 (1985)
50. A. Banholzer, R. Narkowicz, C. Hassel, R. Meckenstock, S. Stienen, O. Posth, D. Suter, M. Farle, J. Lindner, Visualization of spin dynamics in single nanosized magnetic elements. Nanotechnology **22**, 295713 (2011)
51. S.S. Kalarickal, P. Krivosik, M. Wu, C.E. Patton, M.L. Patton, M.L. Schneider, P. Kabos, T.J. Silva, J.P. Nibarger, Ferromagnetic resonance linewidth in metallic thin films: comparison of measurement methods. J. Appl. Phys. **99**, 093909 (2006)
52. G. Woltersdorf, B. Heinrich, Two-magnon scattering in a self-assembled nanoscale network of misfit dislocations. Phys. Rev. B **69**, 188417 (2004)
53. L. Lei, J. Young, W. Mingzhong, C. Mathieu, M. Hadley, P. Krivosik, N. Mo, Tuning of magnetization relaxation in ferromagnetic thin films through seed layers. Appl. Phys. Lett. **100**(2), 022403 (2012)
54. P. Wigen, M. Roukes, P. Hammel, in *Ferromagnetic Resonance Force Microscopy*. vol 101, ed. by B. Hillebrands, A. Thiaville, Spin Dynamics in Confined Magnetic Structures III, Topics in Applied Physics, (Springer, Berlin, 2006), pp. 105–136
55. F. Schreiber, M. Hoffmann, O. Geisau, J. Pelzl, Investigation of the photothermally modulated ferromagnetic resonance signal from magnetostatic modes in yttrium iron garnet films. Appl. Phys. A Mater. Sci. Process. **57**, 545 (1993)
56. R. Meckenstock, Invited review article: Microwave spectroscopy based on scanning thermal microscopy: resolution in the nanometer range. Rev. Sci. Instrum. **79**, 041101 (2008)
57. H. Mahdjour, W.G. Clark, K. Baberschke, High-sensitivity broad-band microwave spectroscopy with small nonresonant coils. Rev. Sci. Instrum. **57**, 1100 (1986)
58. K.D. Bures, K. Baberschke, S.E. Barnes, Electron-Spin-Resonance insitu with a Josephson tunnel jucnction. J. Magnetism Magn. Mater. **54**(Part 3), 1415 (1986)

59. P. Landeros, D.L. Mills, Spin waves in periodically perturbed films. Phys. Rev. B **85**, 054424 (2012)
60. F.M. Romer, M. Moller, K. Wagner, L. Gathmann, R. Narkowicz, H. Zahres, B.R. Salles, P. Torelli, R. Meckenstock, J. Lindner, M. Farle, In situ multifrequency ferromagnetic resonance and x-ray magnetic circular dichroism investigations on Fe/GaAs(110): Enhanced g-factor. Appl. Phys. Lett. **100**, 092402 (2012)
61. S.S. Kalarickal, M. Nan, P. Krivosik, C.E. Patton, Ferromagnetic resonance linewidth mechanisms in polycrystalline ferrites: Role of grain-to-grain and grain-boundary two-magnon scattering processes. Phys. Rev. B **79**, 094427 (2009)
62. A.A. Tulapurkar, Y. Suzuki, A. Fukushima, H. Kubota, H. Maehara, K. Tsunekawa, D.D. Djayaprawira, N. Watanabe, S. Yuasa, Spin-torque diode effect in magnetic tunnel junctions. Nature **438**(7066), 339–342 (2005)
63. J.C. Sankey, P.M. Braganca, A.G.F. Garcia, I.N. Krivorotov, R.A. Buhrman, D.C. Ralph, Spin-transfer-driven ferromagnetic resonance of individual nanomagnets. Phys Rev Lett **96**, 227601 (2006)
64. J.N. Kupferschmidt, S. Adam, P.W. Brouwer, Theory of the spin-torque-driven ferromagnetic resonance in a ferromagnet/normal-metal/ferromagnet structure. Phys. Rev. B **74**(13), 134416 (2006)
65. A. Alexey, Gerrit E. W. Bauer, A. Brataas, Current-driven ferromagnetic resonance, mechanical torques, and rotary motion in magnetic nanostructures. Phys. Rev. B **75**, 014430 (2007)
66. G.D. Fuchs, J.C. Sankey, V.S. Pribiag, L. Qian, P.M. Braganca, A.G.F. Garcia, E.M. Ryan, Z.-P. Li, O. Ozatay, D.C. Ralph, R.A. Buhrman, Spin-torque ferromagnetic resonance measurements of damping in nanomagnets. Appl. Phys. Lett. **91**, 062507 (2007)
67. W. Chen, J.-M.L. Beaujour, G. de Loubens, A.D. Kent, J.Z. Sun, Spin-torque driven ferromagnetic resonance of co/ni synthetic layers in spin valves. Appl. Phys. Lett. **92**, 012507 (2008)
68. W. Chen, G. de Loubens, J.-M. L. Beaujour, A.D. Kent, J.Z. Sun, Finite size effects on spin-torque driven ferromagnetic resonance in spin valves with a Co/Ni synthetic free layer. J. Appl. Phys. **103**(7), 07A502 (2008)
69. J.C. Sankey, Y.-T. Cui, J.Z. Sun, J.C. Slonczewski, R.A. Buhrman, D.C. Ralph, Measurement of the spin-transfer-torque vector in magnetic tunnel junctions. Nat. Phys. **4**, 67–71 (2008)
70. W. Chen, G. de Loubens, J.-M.L. Beaujour, J.Z. Sun, A.D. Kent, Spin-torque driven ferromagnetic resonance in a nonlinear regime. Appl. Phys. Lett. **95**, 172513 (2009)
71. W.H. Rippard, A.M. Deac, M.R. Pufall, J.M. Shaw, M.W. Keller, S.E. Russek, G.E.W. Bauer, C. Serpico, Spin-transfer dynamics in spin valves with out-of-plane magnetized CoNi free layers. Phys. Rev. B **81**, 014426 (2010)
72. C. Wang, Y.-T. Cui, J.A. Katine, R.A. Buhrman, D.C. Ralph, Time-resolved measurement of spin-transfer-driven ferromagnetic resonance and spin torque in magnetic tunnel junctions. Nat. Phys. **7**, 496 (2011)
73. R.D. McMichael, M.D. Stiles, Magnetic normal modes of nanoelements. J. Appl. Phys. **97**, 10J901 (2005)
74. J.M. Shaw, T.J. Silva, M.L. Schneider, R.D. McMichael, Spin dynamics and mode structure in nanomagnet arrays: effects of size and thickness on linewidth and damping. Phys. Rev. B **79**, 184404 (2009)
75. H.T. Nembach, J.M. Shaw, T.J. Silva, W.L. Johnson, S.A. Kim, R.D. McMichael, P. Kabos, Effects of shape distortions and imperfections on mode frequencies and collective linewidths in nanomagnets. Phys. Rev. B **83**, 094427 (2011)
76. P.W. Anderson, H. Suhl, Instability in the motion of ferromagnets at high microwave power levels. Phys. Rev. **100**, 1788 (1955)
77. Y.K. Fetisov, C.E. Patton, V.T. Synogach, Nonlinear ferromagnetic resonance and foldover in yttrium iron garnet thin films-inadequacy of the classical model. IEEE Trans. Magn. **35**, 4511–4521 (1999)
78. M.T. Weiss, Microwave and low-frequency oscillation due to resonance instabilities in ferrites. Phys. Rev. Lett. **1**, 239–241 (1958)

79. W.H. Rippard, M.R. Pufall, S. Kaka, S.E. Russek, T.J. Silva, Direct-current induced dynamics in $Co_{90}Fe_{10}/Ni_{80}Fe_{20}$ point contacts. Phys. Rev. Lett. **92**, 027201 (2004)
80. W.K. Hiebert, L. Lagae, J. De Boeck, Spatially resolved ultrafast precessional magnetization reversal. Phys. Rev. B **68**, 020402(R) (2003)
81. M. Buess, R. Hoellinger, T. Haug, K. Perzlmaier, U. Krey, D. Pescia, M.R. Scheinfein, D. Weiss, C.H. Back, Fourier transform imaging of spin vortex eigenmodes. Phys. Rev. Lett. **93**, 077207 (2004)
82. F. Hoffmann, G. Woltersdorf, K. Perzlmaier, A.N. Slavin, V.S. Tiberkevich, A. Bischof, D. Weiss, C.H. Back, Mode degeneracy due to vortex core removal in magnetic disks. Phys. Rev. B **76**, 014416 (2007)
83. K.Y. Guslienko, A.N. Slavin, V. Tiberkevich, S.-K. Kim, Dynamic origin of azimuthal modes splitting in vortex-state magnetic dots. Phys. Rev. Lett. **101**, 247203 (2008)
84. M. Covington, T.M. Crawford, G.J. Parker, Time-resolved measurement of propagating spin waves in ferromagnetic thin films. Phys. Rev. Lett. **89**, 237202 (2002)
85. K. Perzlmaier, G. Woltersdorf, C.H. Back, Observation of the propagation and interference of spin waves in ferromagnetic thin films. Phys. Rev. B **77**, 054425 (2008)
86. I. Neudecker, G. Woltersdorf, B. Heinrich, T. Okuno, G. Gubbiotti, C.H. Back, Comparison of frequency, field, and time domain ferromagnetic resonance methods. J. Mag. Mag. Mat. **307**, 148–156 (2006)
87. I. Neudecker, K. Perzlmaier, F. Hoffmann, G. Woltersdorf, M. Buess, D. Weiss, C.H. Back, Modal spectrum of permalloy disks excited by in-plane magnetic fields. Phys. Rev. B **73**, 134426 (2006)
88. L. Berger, Emission of spin waves by a magnetic multilayer traversed by a current. Phys. Rev. B **54**, 9353 (1996)
89. J.C. Slonczewski, Current-driven excitation of magnetic multilayers. J. Magn. Magn. Mater. **159**, 1 (1996)
90. S.I. Kiselev, J.C. Sankey, I.N. Krivorotov, N.C. Emley, R.J. Schoelkopf, R.A. Buhrman, D.C. Ralph, Microwave oscillations of a nanomagnet driven by a spin-polarized current. Nature **425**, 380 (2003)
91. I.N. Krivorotov, N.C. Emley, J.C. Sankey, S.I. Kiselev, D.C. Ralph, R.A. Buhrman, Time-domain measurements of nanomagnet dynamics driven by spin-transfer torques. Science **307**, 228 (2005)
92. T. Kimura, Y. Otani, J. Hamrle, Switching magnetization of a nanoscale ferromagnetic particle using nonlocal spin injection. Phys. Rev. Lett. **96**, 037201 (2006)
93. Y. Tserkovnyak, A. Brataas, G.E.W. Bauer, Enhanced gilbert daming in thin ferromagnetic films. Phys. Rev. Lett. **88**, 117601 (2002)
94. R. Urban, G. Woltersdorf, B. Heinrich, Gilbert damping in single and multilayer ultrathin films: Role of interfaces in nonlocal spin dynamics. Phys. Rev. Lett. **87**, 217204 (2001)
95. B. Heinrich, Y. Tserkovnyak, G. Woltersdorf, A. Brataas, R. Urban, G.E. Bauer, Dynamic exchange coupling in magnetic bilayers. Phys. Rev. Lett. **90**, 187601 (2003)
96. M.D. Stiles, A. Zangwill, Anatomy of spin-transfer torque. Phys. Rev. B **66**(1), 014407 (2002)
97. O. Mosendz, G. Woltersdorf, B. Kardasz, B. Heinrich, C.H. Back, Magnetization dynamics in the presence of pure spin currents in magnetic single and double layers in spin ballistic and diffusive regimes. Phys. Rev. B **79**, 224412 (2009)
98. K. Khazen, H.J. von Bardeleben, J.L. Cantin, L. Thevenard, L. Largeau, O. Mauguin, A. Lemaître, Ferromagnetic resonance of $Ga_{0.93}Mn_{0.07}As$ thin films with constant Mn and variable free-hole concentrations. Phys. Rev. B **77**, 165204 (2008)
99. C. Bihler, M. Althammer, A. Brandlmaier, S. Geprägs, M. Weiler, M. Opel, W. Schoch, W. Limmer, R. Gross, M.S. Brandt, S.T.B. Goennenwein, $Ga_{1-x}Mn_xAs$ /piezoelectric actuator hybrids: A model system for magnetoelastic magnetization manipulation. Phys. Rev. B **78**, 045203 (2008)
100. D. Chiba, M. Sawicki, Y. Nishitani, Y. Nakatani, F. Matsukura, H. Ohno, Magnetization vector manipulation by electric fields. Nature **455**, 515 (2008)

101. F. Hoffmann, G. Woltersdorf, W. Wegscheider, A. Einwanger, D. Weiss, C.H. Back, Mapping the magnetic anisotropy in (Ga, Mn)As nanostructures. Phys. Rev. B **80**, 054417 (2009)
102. J. Wenisch, C. Gould, L. Ebel, J. Storz, K. Pappert, M.J. Schmidt, C. Kumpf, G. Schmidt, K. Brunner, L.W. Molenkamp, Control of magnetic anisotropy in (Ga, Mn)As by lithography-induced strain relaxation. Phys. Rev. Lett. **99**, 077201 (2007)

http://www.springer.com/978-3-642-32041-5

Magnetic Nanostructures
Spin Dynamics and Spin Transport
Zabel, H.; Farle, M. (Eds.)
2013, XVI, 268 p., Hardcover
ISBN: 978-3-642-32041-5